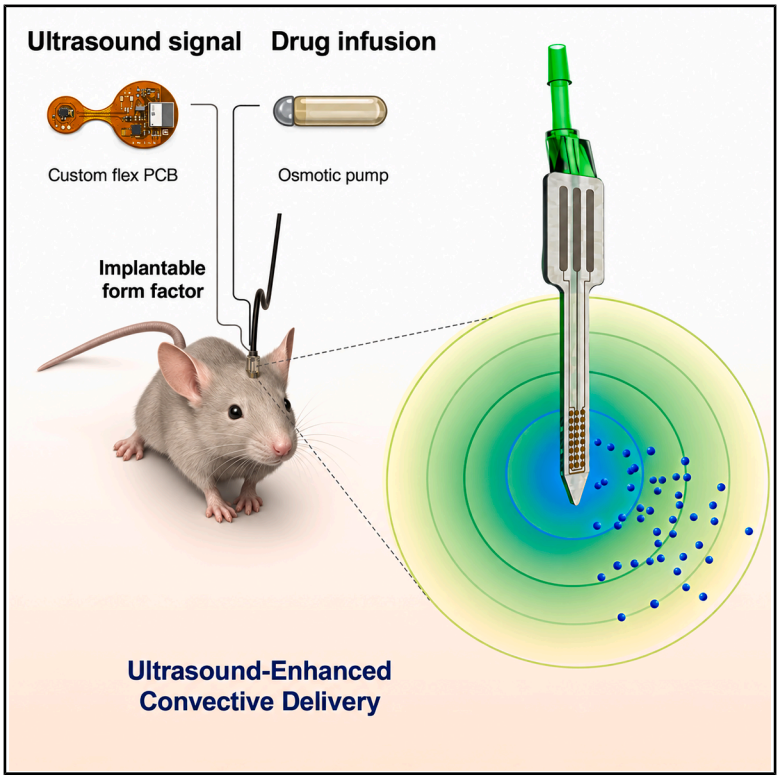
Device

Article

Long-term ultrasound-enhanced convective injection device for neural drug delivery

Graphical abstract



Highlights

- A 24-element ultrasound array integrates with a printed neural-delivery cannula
- Wireless power and control support a 20-h phantom delivery experiment
- Ultrasound roughly doubles dye-distribution area in one paired phantom run
- LUCID increases acute brain contrast-distribution volume by 40% vs. syringe CED

Authors

Jason F. Hou, Sarah B. Ornellas, Michal O. Nowicki, ..., Steve Ramirez, E. Antonio Chiocca, Canan Dagdeviren

Correspondence

canand@media.mit.edu

In brief

Delivering drugs directly into the brain can bypass the blood-brain barrier, but their spread through tissue remains limited. LUCID combines a miniature ultrasound array, an injection channel, and wireless control to improve local distribution. The device increased dye spread during a 20-h phantom experiment and enlarged contrast-agent distribution in mouse brain. These findings support further development toward sustained neural drug delivery, while long-term performance in living tissue remains to be tested.

4 **Validate**
Functional device with real-world testing, ready to scale

Hou et al., 2027, Device *5*, 101333
January 15, 2027 © 2026 Elsevier Inc. All rights are reserved, including those for text and data mining, AI training, and similar technologies.
https://doi.org/10.1016/j.device.2026.101333

CellPress

Please cite this article in press as: Hou et al., Long-term ultrasound-enhanced convective injection device for neural drug delivery, Device (2026), https://doi.org/10.1016/j.device.2026.101333

Device

CellPress

Article

Long-term ultrasound-enhanced convective injection device for neural drug delivery

Jason F. Hou,[1,7] Sarah B. Ornellas,[1,7] Michal O. Nowicki,[2] Jerry Li,[3] Heloise Leblanc,[4] Betul Serra Tulu,[5] David Sadat,[1] Marco Mineo,[2] Steve Ramirez,[6] E. Antonio Chiocca,[2] and Canan Dagdeviren[1,8,*]

[1]Media Lab, Massachusetts Institute of Technology, Cambridge, MA 02139, USA
[2]Harvey Cushing Neuro-oncology Laboratories, Department of Neurosurgery and Center for Tumors of the Nervous System, Mass General Brigham, Boston, MA 02115, USA
[3]Department of Electrical Engineering, Harvard University, Cambridge, MA 02138, USA
[4]Boston University Chobanian and Avedisian School of Medicine, Boston, MA 02218, USA
[5]Department of Mechanical Engineering, Massachusetts Institute of Technology, Cambridge, MA 02139, USA
[6]Psychological & Brain Sciences Department, Boston University, Boston, MA 02215, USA
[7]These authors contributed equally
[8]Lead contact
*Correspondence: canand@media.mit.edu
https://doi.org/10.1016/j.device.2026.101333

THE BIGGER PICTURE Delivering therapeutics to the brain faces two critical barriers: most drugs cannot cross the blood-brain barrier (BBB) due to their size at therapeutic concentrations and *in situ* injection methods require repeated invasive surgeries that risk damaging healthy tissue. Strategies to enhance drug delivery include transcranially disrupting the BBB with remote ultrasound (US), allowing systemically delivered drugs to transiently infiltrate the parenchyma, or injecting drugs locally under constant positive pressure using convection-enhanced delivery (CED). Systemic injection strategies are limited by off-target toxicity, and external US equipment is bulky and resource intensive. While CED enables targeted parenchymal distribution, it remains limited to acute applications with external equipment and poor tissue penetration due to resistance in densely packed neural tissue. Current approaches cannot provide chronic, controlled delivery of therapeutic payloads to the brain without repeated craniotomies and backflow loss. LUCID addresses these challenges by combining ultrasound-enhanced convective delivery with a fully implantable, wirelessly controlled platform that significantly enlarges parenchymal distribution volume relative to syringe-based CED. The platform demonstrates 20 h of continuous wireless operation in a tissue phantom, providing the technical foundation for future programmable, longitudinal therapeutic regimens that eliminate the need for repeated surgical access and expand distribution beyond what pressure-driven infusion alone can achieve.

SUMMARY

Targeted brain delivery remains challenging, as current approaches require repeated craniotomies, tethered equipment, or systemic administration with poor blood-brain barrier (BBB) penetration. Here, we present the long-term ultrasound-enhanced convective injection device (LUCID), a chronic implantable system integrating a flexible 24-element piezoelectric micromachined ultrasound transducer (pMUT) array with a two-photon 3D-printed cannula, wireless-powered PCB, and passive osmotic reservoir for fully implantable, ultrasound-enhanced convective delivery. Ultrasound increases interstitial transport and distribution volumes beyond conventional pressure-driven infusion. We demonstrate payload distribution across an escalating range of BBB exclusion: rhodamine B (479 Da), Gadavist (605 Da; *in vivo*), and TRITC-dextran (~70 kDa; size matched to large therapeutic proteins). By eliminating repeated surgical interventions, LUCID enables longitudinal delivery regimens that locally enhance the distribution of BBB-excluded payloads, with potential applications in brain tumors and neurodegenerative diseases and gene therapy delivery directly to neural circuits. This technology addresses a critical unmet need for minimally invasive, programmable, long-term drug delivery.

All rights are reserved, including those for text and data mining, AI training, and similar technologies.

Please cite this article in press as: Hou et al., Long-term ultrasound-enhanced convective injection device for neural drug delivery, Device (2026), https://doi.org/10.1016/j.device.2026.101333

INTRODUCTION

The brain remains the most pharmacologically protected organ in the body. The blood-brain barrier (BBB) excludes the great majority of small-molecule drugs and effectively all large biologics from entering the parenchyma at therapeutic concentrations.[1,2] severely limiting treatment of central nervous system (CNS) pathologies including, glioblastoma, and other oncologic and neurodegenerative disorders. The same constraint limits translational neuroscience itself: chronic delivery of optogenetic, chemogenetic, and gene-therapy payloads—increasingly central tools for circuit dissection[3,4]—currently demands repeated craniotomies that compound surgical risk and tissue scarring. Together, these clinical and research needs motivate a chronic, targeted, and minimally invasive drug-delivery platform capable of distributing therapeutic payloads across functionally relevant brain volumes.

Glioblastoma (GBM), the most common and most aggressive primary brain malignancy in adults, illustrates how acutely these constraints limit clinical practice. The standard of care is the Stupp protocol, established two decades ago, which combines maximal safe surgical resection with concomitant temozolomide chemotherapy and 60 Gy of fractionated radiotherapy, followed by six cycles of adjuvant temozolomide.[5] Even so, the median overall survival remains 2 years for GBMs with a methylated MGMT promoter and less than that for those without MGMT promoter methylation. Almost invariably, tumor recurrence is nearly universal at the resection margin.[5] Surgery itself, however, opens a therapeutic window: the post-resection cavity provides direct access to peritumoral parenchyma, bypassing the BBB. A diverse and rapidly expanding set of post-operative delivery technologies has emerged to exploit this window, supporting payloads as varied as small-molecule chemotherapeutics, oncolytic viruses, chimeric antigen receptor (CAR) T cells, cytokines, and gene therapies. These technologies include carmustine-impregnated biodegradable wafers (e.g., GLIADEL) implanted into the resection cavity at the end of surgery,[6,7] sustained-release polymer and hyaluronic acid hydrogels carrying chemotherapeutics or biologics,[8,9] catheter-based locoregional CAR T-cell delivery,[10] alternating electric field stimulation devices (tumor treating fields, Optune),[11] and implanted catheter-pump systems for repeated chemotherapy dosing. Each is well suited to a particular dosing regimen and payload class, yet none combines large-volume parenchymal distribution, programmable temporal control, and fully implanted, wireless operation in a single platform.

Convection-enhanced delivery (CED), first demonstrated in the 1990s[2] infuses therapeutics under continuous positive pressure through a catheter to bypass the BBB and distribute molecules across centimeter-scale brain volumes. CED has since progressed to clinical trials for glioma, GDNF infusion in Parkinson's disease, and gene therapy,[12,13] yet two limitations persist. First, the high backflow and tissue resistance of densely packed parenchyma cap the achievable distribution volume for a given infusion rate, particularly for high-molecular-weight payloads. Second, almost all current CED implementations are acute: percutaneous catheters tethered to external syringe pumps, inserted at the time of treatment and removed afterward, requiring repeated craniotomies for any longitudinal regimen. Advances in the field include reflux-resistant catheter designs, improved understanding of flow dynamics in brain tissue, image-guided placement, and early exploration of implantable pump-based systems that could support longer-term CED.[14,15] Despite these gains, clinical implementation still faces major barriers: maintaining stable, predictable distribution in anisotropic brain tissue, preventing backflow and catheter-related complications, ensuring long-term implant reliability and infection control, and verifying drug spread in real time during chronic treatment.[14] No chronic, fully implantable CED platform with active flow enhancement is presently available in routine clinical practice.

An emerging strategy for local delivery of therapeutic agents in the brain uses transcranially focused ultrasound (FUS) with intravenously circulating microbubbles to transiently and reversibly open the BBB at a chosen target,[16] allowing systemically administered drugs to extravasate locally. Since the first noninvasive demonstration in rabbits[16] and clinical translation in Alzheimer's disease,[17] the FUS-BBB opening has been applied across a growing range of indications. Recent clinical applications span neurodegenerative disorders, glioma, and other cancers; in addition, due to its synergistic potential with treatments like immunotherapies, the literature increasingly reflects FUS-BBB's broad translational potential.[18–22] However, FUS-BBB is fundamentally a perfusion-enhancement technique; the systemic dose required for therapeutic concentrations within the small treated volume can incur off-target toxicity for many payloads, and the supporting equipment (high-element-count phased arrays, MR or neuronavigation guidance, and anesthesia) is bulky, expensive, and resource intensive.[23] Recent advances have reduced the infrastructure burden of FUS-BBB considerably, as portable, neuronavigation-guided systems with real-time cavitation monitoring have demonstrated safe and feasible BBB opening in Alzheimer's patients outside the MRI suite[24] and sub-$100 transducers have achieved millimeter-precision opening in preclinical models.[25] Nonetheless, none of these platforms support the programmable, repeated bolus regimens that chronic CNS diseases and aggressive tumors such as GBM demand, where sustained therapeutic drug concentrations over extended treatment courses are essential.[26] Neither standard CED nor remote FUS, taken alone, can simultaneously provide local delivery, active flow enhancement, low off-target dose, and chronic implantability.

Ultrasound (US) has traditionally been confined to diagnostic imaging within clinical settings, but over the past two decades, it has extended its use into non-clinical, portable form factors, such as wearables, implantables, and augmented reality (AR) and virtual reality (VR) interfaces.[27–31] US-enhanced drug delivery rises as a suitable strategy for programmable local transport of therapeutic payloads in brain tissue, with implantable miniaturized US transducers leading the race for a minimally invasive form factor. On the mechanistic end, US-driven acoustic streaming has been shown to enhance intratumoral drug distribution by up to 500% over CED alone in brain-mimicking phantoms.[32] Acoustic streaming in fluids may arise through classical mechanisms such as Eckart streaming, in which attenuation of propagating acoustic waves generates bulk directional flow, and Rayleigh streaming, where viscous boundary layer effects produce

Please cite this article in press as: Hou et al., Long-term ultrasound-enhanced convective injection device for neural drug delivery, Device (2026), https://doi.org/10.1016/j.device.2026.101333

vortical flow patterns that enhance local mixing and transport near interfaces.[33] In soft porous tissue, however, recent theory and experiments indicate that US-enhanced transport should be understood as tissue-scale convective delivery rather than as classical streaming in a pure fluid, with the greatest benefit occurring when baseline pump-driven flow is weak or when large, slowly diffusing payloads require additional transport beyond diffusion.[32,34] Needle-integrated US transducers exploit acoustic streaming to drive directional perfusion and drug penetration beyond a weak, pump-driven infusion in intratumoral immunotherapy applications.[35] At the cannula tip, oscillatory pressure converts into directional acoustic streaming,[33,36] which drives convective transport on length scales matched to brain microenvironments. On the form factor end, capacitive micromachined ultrasound transducers (CMUTs)[37] and piezoelectric micromachined US transducers[38,39] (pMUTs) can be fabricated on flexible substrates, generate $\geq$1 MPa local pressure at submillimeter form factors, and in the case of biocompatible piezoceramics such as potassium sodium niobate (KNN), operate without an electrochemically active interface, supporting long-term stability.[30] Group precedents have established miniaturized intracerebral drug-delivery implants[40] and prior work has shown that flexible KNN-based pMUTs can stimulate deep-brain neurons *in vivo*.[30] To our knowledge, however, no platform has integrated active acoustic flow enhancement with implantable, wirelessly powered, programmable convective delivery.

Here, we report the long-term ultrasound-enhanced convective injection device (LUCID), a flexible, fully implantable system that combines a 24-element KNN-on-SU-8 pMUT array, an *in situ* two-photon-printed microfluidic cannula, a passive osmotic-pump reservoir, and a custom wirelessly powered drive PCB with Bluetooth Low Energy (BLE) control. We characterize the array's acoustic output in water ($\sim$0.8 MPa peak to peak in the voltage sweep and up to $\sim$1 MPa peak to peak near the tip at 300 kHz), validate the streaming mechanism by particle tracking, demonstrate atraumatic insertion and thermal safety, and show that US-ON operation significantly increases dye-distribution kinetics *in vitro* and gadolinium-distribution volume *in vivo* by MRI in the mouse brain. The platform thereby establishes a building block for programmable, longitudinal therapeutic regimens for CNS delivery.

Table 1 compares the intraparenchymal delivery strategies with other routes for delivery to the CNS.

RESULTS

Design and architecture of LUCID

We designed LUCID to combine within a single flexible, fully implantable form factor the main functional elements for an effective brain parenchyma delivery: local convective infusion of a drug, active acoustic streaming enhancement, a passive long-duration reservoir, and wireless control. The device is intended to be implanted at the time of resection or stereotactic placement, and the cannula tip is positioned within the target parenchyma. An applied ultrasonic field at the cannula tip drives local convection that enlarges the effective distribution volume of an infused payload, while the same oscillatory pressure transiently perturbs the surrounding tissue and increases interstitial transport within the parenchyma (Figure 1A).

Architecturally, LUCID integrates a 24-element pMUT array, built from the biocompatible piezoceramic KNN sandwiched electrodes and encapsulated by SU-8 polymer layers. It incorporates an *in situ* two-photon-printed microfluidic injection cannula, which can be connected to a 0.5-mm internal diameter (ID) silicone tubing via a barbed tube inlet (Figure 1B). The microfluidic cannula is printed directly onto the device after pMUT release and routes infusate from a liquid drug reservoir to the cannula outlet at the US-active region of the array. Different configurations of the pump and driver allow for acute delivery with common benchtop equipment such as a syringe pump and a function generator, or chronic delivery with an implantable custom PCB, which hosts a BLE-capable system-in-package (SIP) with an integrated boost converter and piezo driver, a Li-ion battery, and a resonant-inductive charging coil, allowing the device to be operated and recharged through intact tissue without external connections (Figure 1C). An anisotropic conductive film (ACF) cable with printed conductive traces and a flexible silicone tube allow LUCID to be adaptively connected to both benchtop and miniaturized systems (Figure 1D). A coin-sized flexible PCB and a small osmotic pump (Alzet) comprise the chronic delivery system, which can be encapsulated and fully implanted (Figure 1E). The pMUT array is fabricated on a flexible polymer substrate and forms the active acoustic surface; each element comprises a thin KNN piezoelectric membrane suspended over a sealed air cavity with a larger cavity comprising the cross-section of the microfluidic channel (Figure 1F). The minimum dimension is 150 μm in thickness, and the maximum dimension is 933 μm in width.

LUCID combines *in situ* two-photon 3D printing with wafer-level microfabrication

The pMUT array was fabricated using a top-down process beginning from a multilayer thin-film stack (KNN/Pt/ZnO on SiO_2/Si) that was lithographically patterned, transferred onto a polymer encapsulation layer, and sealed with an air-cavity backing (full process in methods section, Figure S1).[30] A 24-element layout was chosen to maximize the total radiating area while preserving a flexible, conformable head footprint. The microfluidic injection cannula was subsequently printed directly onto the device on wafer by two-photon lithography (Figure 2A; UpNano NanoOne), enabling fluid-tight integration with sub-micrometer registration to the array. Subsequently, the entire structure is released by chemically dissolving a release layer between the device and the silicon wafer surface (Figure S2).

Acoustic characterization of LUCID

For the initial acoustic resonance characterization of LUCID, the array of pMUTs was tested while submerged in deionized (DI) water. Ultrasonic transducers' characterization under water serve as a proxy for *in vivo* performance of the transducers due to similar speed of sound (1,500 m/s in water $\times$ 1,560 m/s in brain tissue, in contrast with 343 m/s in air).[43] Electrical impedance spectroscopy of an assembled device submerged in water revealed a resonance frequency of 352.8 kHz and an

Please cite this article in press as: Hou et al., Long-term ultrasound-enhanced convective injection device for neural drug delivery, Device (2026), https://doi.org/10.1016/j.device.2026.101333

Table 1. Comparison of intraparenchymal drug delivery strategies

Method	Advantage	Biocompatibility with brain tissue	Administration mode	Limitation
Systemic delivery (IV/oral)	Non-invasive or minimally invasive; clinically established and scalable; suitable for repeated chronic dosing	Systemically biocompatible; limited interaction with brain tissue due to BBB exclusion	Intravenous injection or oral administration	Most biologics and large-molecule therapeutics cannot effectively cross the BBB[1]; risk of systemic off-target toxicity and high peripheral exposure
Convection-enhanced delivery	Uses a positive pressure gradient that improves distribution of agents into tissue	Big mechanical mismatch (steel syringe)	Acute injection	To avoid reflux, low flow rates and smaller diameter syringes are used, but backflow is still reported. Infusion volume/duration of treatment becomes a limitation[15]
Intrathecal delivery	Bypasses the BBB through CSF; enables delivery of biologics and nucleic acids to CNS compartments	Generally well tolerated; repeated lumbar or ventricular access may cause irritation or infection risk	Repeated lumbar puncture or implanted intrathecal catheter/pump	CSF exposure does not guarantee deep-brain parenchymal penetration and distribution is constrained by anatomy and CSF clearance[41]
Implantable pumps/reservoir systems	Enables chronic and programmable local drug administrations with reduced need for repeated surgeries.	Chronic implants may induce fibrosis, inflammation, infection risk, or mechanical mismatch with soft neural tissue	Surgically implanted reservoir or pump connected to catheter	Limited tissue penetration and distribution volume; device complexity, refill requirements, and long-term foreign body response
Passive implanted depots	Sustained local release without active pumping or external control; reduced dosing frequency[6,9]	Biocompatibility depends on material degradation profile; risk of scar tissue formation or inflammatory response from degradation by-products	Surgically implanted biodegradable or non-biodegradable depot; chronic delivery	Passive diffusion limits spatial distribution and dosing precision; therapy difficult to adjust after implantation; non-biodegradable variants risk fibrous encapsulation
Active implantable systems	Wirelessly controlled, programmable, and longitudinal therapeutic delivery; eliminates need for repeated surgical access	Improved compliance possible with soft/flexible bioelectronic materials; chronic implantation still risks fibrosis	Chronically implanted system with active pumping or actuation; wireless activation	Increased device complexity, power requirements, and long-term reliability challenges; surgical implantation required
Intranasal delivery	Non-invasive route that may partially bypass BBB via olfactory and trigeminal pathways	Generally well tolerated with minimal direct tissue disruption	Nasal spray or intranasal administration; chronic repeated dosing	Low and variable delivery efficiency; limited dosing volume; inconsistent and poorly controlled transport to deep-brain regions
Intravascular delivery + US/microbubble (MB) BBB disruption	Local and transient BBB disruptions allow drugs not usually permeable to reach the tumor	MBs are absorbable within minutes	Acute injection and wearable US array; chronic US array possible[42] but leaves permanent 6 × 6cm cranial window	Does not address off-target toxicity of intravascularly delivered agents. Resource intensive (e.g., need for MRI-guidance or neuronavigation)

CSF, cerebrospinal fluid.

anti-resonance peak at 487.0 kHz after subtraction of a parallel cable capacitance contributed by the ACF cable and PCB traces of ≈193.5 pF that otherwise dominates the raw response (Figure 2B and inset). Scanning laser Doppler vibrometer (LDV) measures velocity amplitudes across a range of frequencies in a grid of points across the device surface while submerged in water (Figure S3). Devices were driven by a chirp signal in the 50 kHz–2 MHz range, and the peak resonance frequency of each array element was collected. After averaging and normalizing the converted peak displacement across the 24-element arrays of eight devices for the resonance sweep, a resonance frequency of 306 kHz is found, and it is in

Please cite this article in press as: Hou et al., Long-term ultrasound-enhanced convective injection device for neural drug delivery, Device (2026), https://doi.org/10.1016/j.device.2026.101333

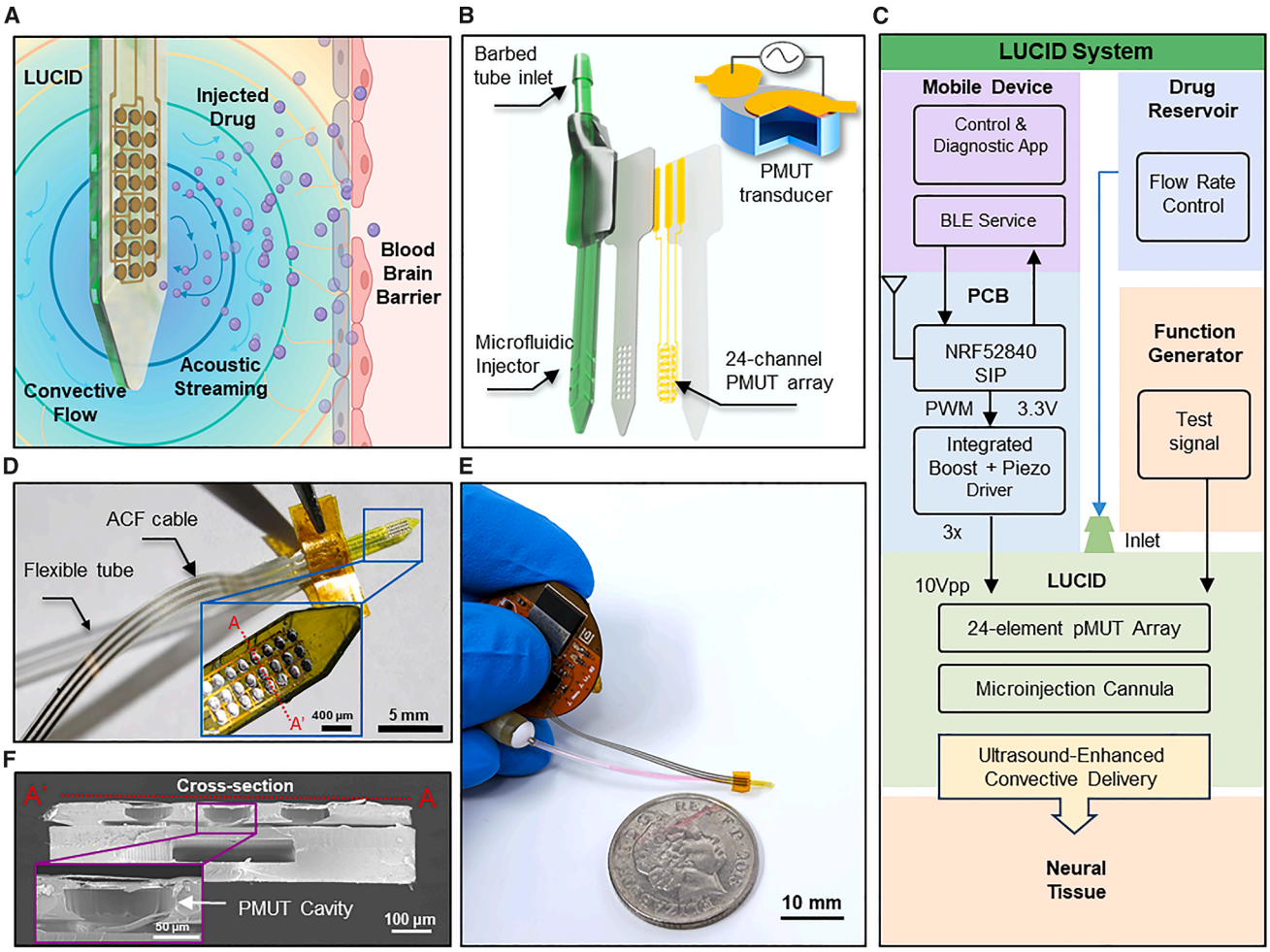


Figure 1. Description of LUCID device

(A) Mechanism of action of LUCID in neural tissue. Payload infused through the cannula is distributed within the parenchyma by ultrasound-enhanced convective flow, which augments interstitial transport beyond that achievable by pressure-driven infusion alone. Note that delivery is intraparenchymal and, therefore, bypasses the blood-brain barrier by construction.

(B) Exploded rendering of LUCID elements and internal view of single pMUT transducer (top right).

(C) Schematic of LUCID electronic powering system, including wireless actuation through a mobile device (left) or test actuation with a function generator (right).

(D) Photograph of LUCID device, with microscopic detail of pMUT array (inset).

(E) Photograph of LUCID device coupled to a custom PCB and an osmotic pump reservoir (Alzet 1003D, 100 µL at a nominal 1 µL h^{-1}), a manufacturer specification sufficient for several days of continuous infusion; longer-duration pump models are available for multi-week regimens.

(F) SEM picture of cross section of pre-cleaved LUCID device, with detail of pMUT cavity (inset).

See also Figures S1 and S2. Scale bars: 5 mm in (D) and 400 µm in (inset of D); 10 mm in (E); 100 µm in (F) and 50 µm in (inset of F).

close proximity to the simulated peak resonance of 300 kHz, predicted by COMSOL Multiphysics v.6.1 (COMSOL AB, Sweden), which models the multiphysics interactions between the pMUT layer-by-layer geometries, material properties, piezoelectric thin-film actuation, and resulting acoustic properties (Figure 2C). Parameters for the 3D simulated model can be found in Table S1. Spatially reconstructed LDV scans of an array driven at resonance with 10 V_{pp} showed similar out-of-plane displacement across the eight elements sampled in the displacement map, with a single-element peak and 3D profile that matched the simulated single-pMUT mode shape and displacement magnitude of 860 nm (Figure 2D). LDV measurements of all 24 elements illustrate in-phase actuation of the majority of the elements simultaneously (Figure S4). Per-element displacements scaled approximately linearly with the drive voltage from 2 to 10 V_{pp} (Figures 2E and 2F): the peak membrane displacement seen across the scanned array rose from 189 nm at 2 V_{pp} to 387 nm (4 V_{pp}), 617 nm (6 V_{pp}), 838 nm (8 V_{pp}), and 956 nm at 10 V_{pp}, thus corresponding to a mean slope of $\approx$96 nm/V_{pp} across the bench-drive range tested. The electrical-impedance resonance (352.8 kHz), mean LDV displacement resonance (306 kHz), and simulated displacement resonance (300 kHz) are distinct characterizations. Hydrophone pressure measurements used a 300-kHz drive; this

Please cite this article in press as: Hou et al., Long-term ultrasound-enhanced convective injection device for neural drug delivery, Device (2026), https://doi.org/10.1016/j.device.2026.101333

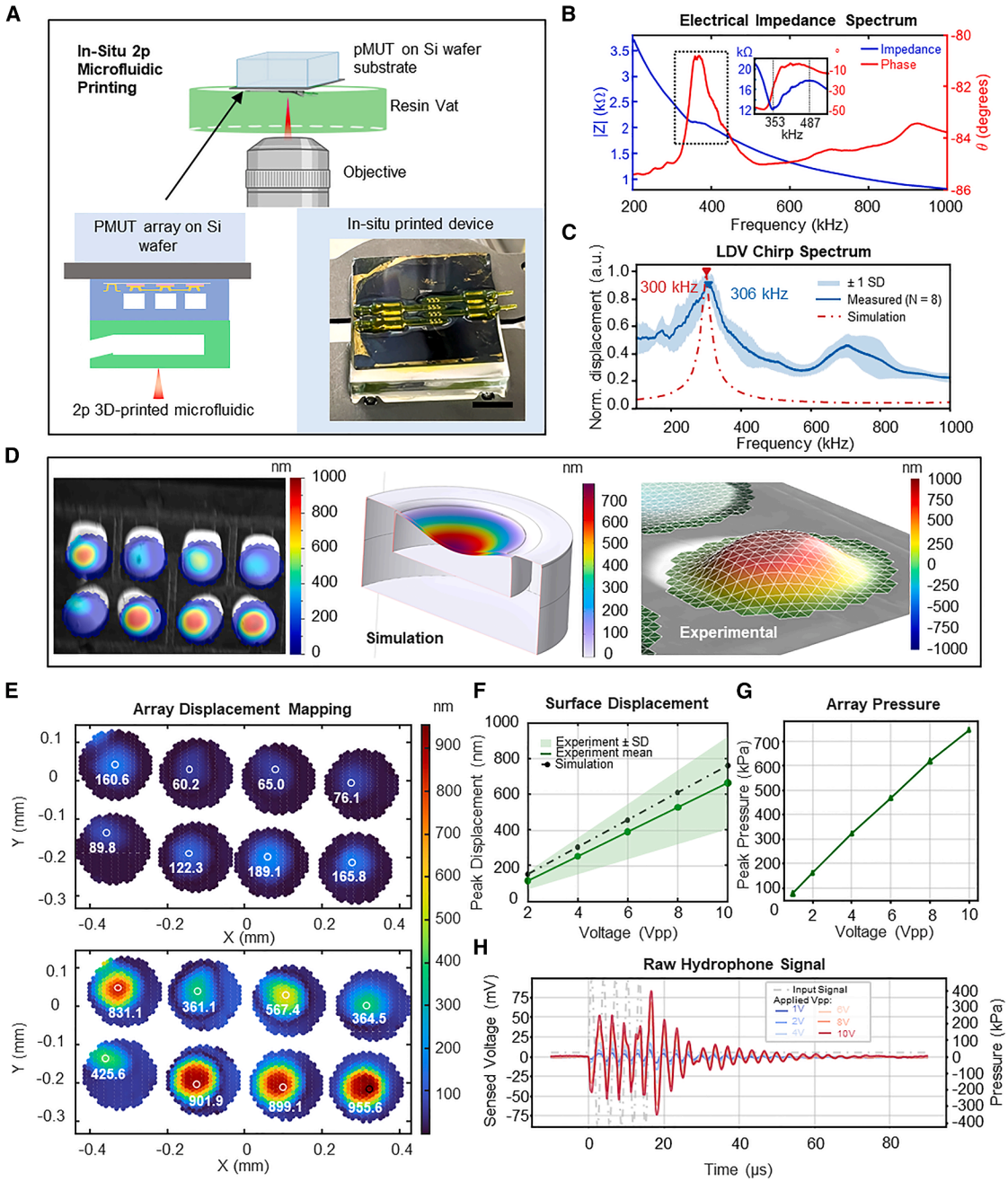


Figure 2. Acoustic characterization of LUCID device

(A) Schematics of *in situ* two-photon 3D printing of microfluidic devices. Photograph of wafer with 4 printed devices (inset). Scale bar, 5 mm.

(B) Electrical impedance of a LUCID device in water. The device was assembled to ACF cable and PCB. Detail of electrical impedance with subtracted values of ACF cable (inset).

(C) Resonance behavior of LUCID device when driven by a chirp signal, measured experimentally in laser Doppler vibrometer (LDV) and simulated in COMSOL. The mean LDV displacement resonance is 306 kHz and the simulated resonance is 300 kHz; the electrical-impedance resonance in (B) is 352.8 kHz. Resonance sweep: n = 8 devices, each containing 24 pMUT elements. Shaded band represents measured resonance sweep ± SD.

(D) Displacement of pMUT membranes. LDV measurement of 8 pMUT elements driven at resonance at $10V_{pp}$ (left); COMSOL simulation of a single pMUT (center) and 3D detail of LDV measurement of a single element (right).

(E) Displacement comparison of 8 pMUT elements when driven by $2V_{pp}$ (top) and $10V_{pp}$ (bottom).

(legend continued on next page)

Please cite this article in press as: Hou et al., Long-term ultrasound-enhanced convective injection device for neural drug delivery, Device (2026), https://doi.org/10.1016/j.device.2026.101333

measured protocol frequency is used for the mechanical index (MI) estimates below, while device-specific frequencies used in other experiments are reported separately.

Calibrated fiber-optic hydrophone measurements in DI water yielded a peak-to-peak pressure of ~800 kPa at 10 V_{pp} and 300 kHz in the voltage sweep (Figure 2G). Figure 2H shows the time-domain waveforms; peak-to-peak pressure is the difference between their positive and negative extrema. The near-tip axial scan is reported separately in Figure 3G.

Acoustic streaming generates targeted convection at the cannula tip

While oscillatory acoustic pressure fields initiate wave propagation, steady-state streaming ultimately arises when this acoustic momentum is transferred to the fluid via bulk viscous attenuation and boundary-layer shear (Rayleigh streaming).[44] To directly capture this resulting convective enhancement, we visualized fluid motion at the cannula outlet using particle-tracking velocimetry (PTV). A video recording system captured particle trajectories of 3.1-μm polystyrene beads within the focal plane of the microscope objective, showing fast streaming of particles in excess of 600 μm per second in opposite directions on different focal planes within the same field of view (Figure S6; Video S1). In the orthogonal velocity components, dipolar flow lobes characteristic of convective flow around the device emerged, spanning −600 to +600 μm/s within ~750 μm of the tip (Figure 3D). Particle tracking measurements are taken from Plane 1 and Plane 2 as outlined in the diagram, while the finite-element simulation depicts Plane 3; line measurements common to Planes 1 and 2 and Plane 3 are compared to link measurement and simulation results (Figure 3A). A finite-element simulation provided validation of both the particle streaming velocity and the general behavior of particle flow, which travels in a vortex spanning a millimeter to the edge of the boundary and wraps around the device (Figure 3C). Associated acoustic pressure field simulations corroborate the origin of these acoustic streaming field patterns as significant inverted pressures are formed on opposite faces of the device that transport the particles from one side to the other (Figure 3B). Particle tracking confirmed that this oscillatory pressure field drove sustained, directional bulk fluid motion at the cannula tip: in-flow and out-flow lanes were aligned with the cannula geometry and produced antisymmetric v_x and v_y profiles (Figure 3E), with sustained particle speeds >100 μm/s persisting across hundreds of micrometers along the central transect (Figure 3F). Both magnitudes and spatial profiles agreed with the finite-element simulation, providing quantitative validation of the streaming mechanism.

The axial hydrophone scan in water reached ~1 MPa peak to peak at the closest sampled positions (nominal distances <50 μm), with pressure decreasing over the ~250-μm scan (Figure 3G). The ~1 MPa value is the largest individual measurement; the experimental mean and scatter are shown separately. Sustained particle velocities of 100–600 μm/s at the cannula outlet are sufficient to drive convective transport that exceeds passive interstitial diffusion of small-molecule and protein-sized payloads at the relevant length scales of brain microenvironments, and to overcome the local backflow along the device shaft that limits conventional CED.[12,13] This streaming field is, therefore, both the mechanistic basis and the design target for the device's downstream *in vitro* and *in vivo* enhancement.

Mechanical, thermal, and *in vitro* dose delivery validation

Translating active flow enhancement into a chronic implantable device imposes three additional constraints: atraumatic insertion, thermal safety under sustained operation, and demonstrable enhancement of bulk dye distribution. We addressed each *in vitro* before approaching animal experiments. For the first constraint, prior work indicates that traumatic insertion is associated with excess local deformation or injury, often reflected by elevated puncture force, tissue dimpling, crack formation, or acute vascular and inflammatory damage.[45] Chronic tissue response is influenced by mechanical mismatch and micromotion, motivating the development of flexible neural interfaces and bioinspired insertion strategies[46–48] Recently, US actuation was also proposed to reduce insertion trauma by lowering insertion forces during implantation.[49] Nevertheless, flexibility can come at the cost of insertability, so an implantation design must balance compliance with sufficient mechanical robustness for entry.[48] Within this context, LUCID showed comparable peak puncturing force to a 26-gauge Hamilton syringe in a tissue-mimicking material while exhibiting a significantly lower force at full insertion.

Insertion mechanics were quantified on an Instron 4411 tensile tester with a 5-N load cell (Figure S5) against 0.6% agarose brain phantoms,[50] comparing LUCID to a 26-gauge Hamilton #701 syringe (Figure 4A; n = 24 LUCID runs across four phantoms, n = 12 syringe controls). Force-time profiles involved four phases: (1) prep—when the devices were held in place after reaching the surface of the agarose phantom (50 s); (2) insertion—when the device is inserted (speed 2 mm/min) into the phantom for a total displacement of 5 mm (150 s); (3) hold—when devices rest inside the phantom at peak 5 mm depth with no displacement (100 s), and (4) retraction—when devices are pulled away from the agarose phantom (speed 2 mm/min) for a total dislocation of −5 mm (150 s). Because chronic implantation requires both atraumatic entry and low sustained tissue loading after placement, we analyzed two pre-specified metrics: the peak puncturing force during initial entry into the

(F) Voltage vs. peak displacement comparison between experiment and COMSOL simulation. Peak displacement across the array at the device resonance was 189 nm (2 V_{pp}), 387 nm (4 V_{pp}), 617 nm (6 V_{pp}), 838 nm (8 V_{pp}), and 956 nm (10 V_{pp}), n = 8 elements per array, scaling approximately linearly at ≈96 nm/V_{pp}. Shaded band represents experiment peak displacement ± SD.

(G) Hydrophone peak-to-peak pressure vs. drive voltage in deionized water at 300 kHz, reaching ~800 kPa at 10 V_{pp}.

(H) Time-domain hydrophone waveforms at the indicated drive voltages; the pressure axis shows signed instantaneous pressure, and the positive-to-negative span corresponds to the peak-to-peak quantity in (G). See also Figures S1–S4; Table S1.

Please cite this article in press as: Hou et al., Long-term ultrasound-enhanced convective injection device for neural drug delivery, Device (2026), https://doi.org/10.1016/j.device.2026.101333

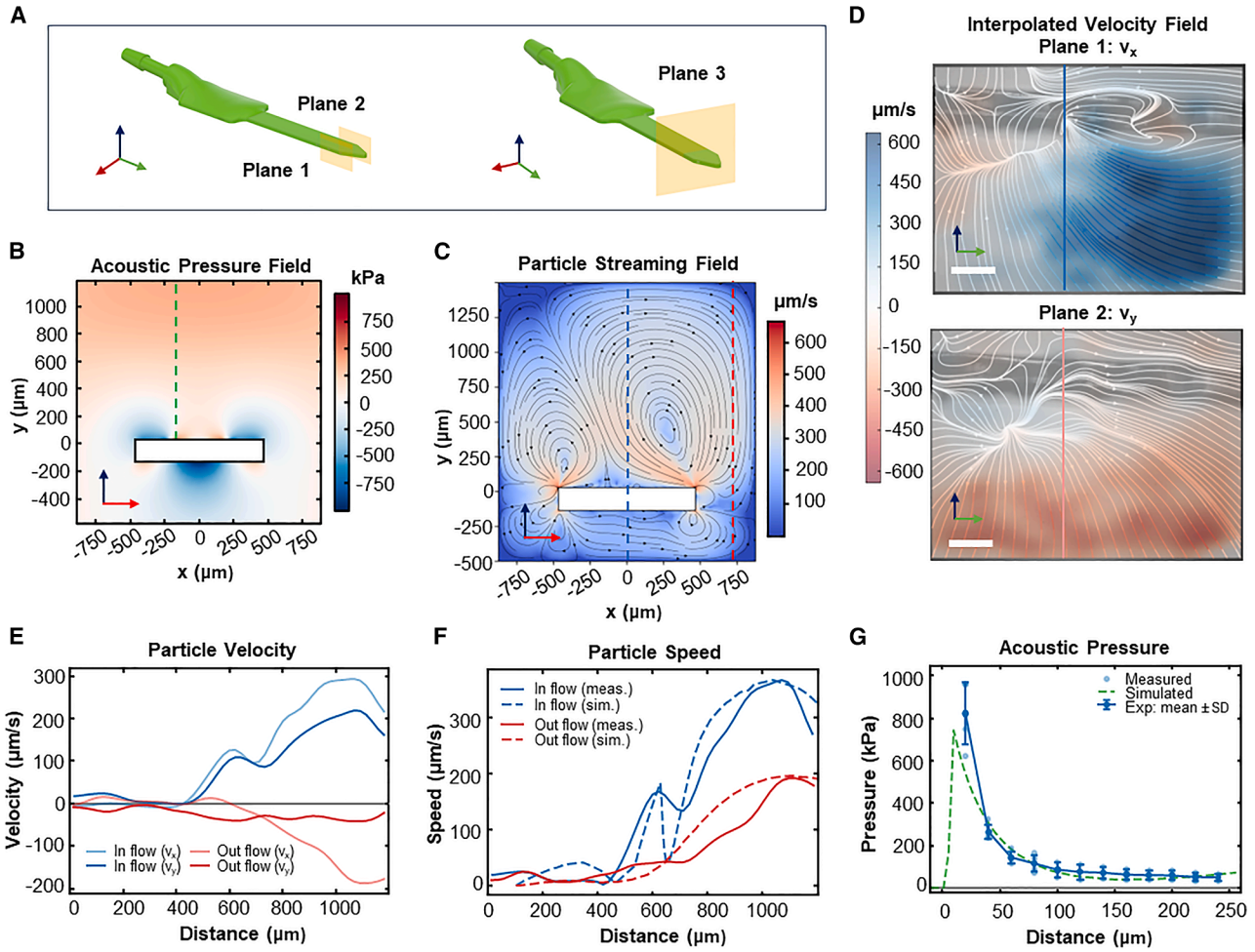


Figure 3. Acoustic pressure and streaming near the LUCID cannula

(A) Three-plane schematic of the imaging volume relative to the LUCID cannula outlet, with two orthogonal plane orientations (Plane 1, Plane 2) used for image-based particle tracking and one parallel plane (Plane 3) used for acoustic pressure and particle streaming measurements.

(B) Simulated acoustic pressure field of the LUCID pMUT/cannula geometry in water; the color scale shows signed pressure. This field map is distinct from the measured axial pressure profile in (G).

(C) Simulated particle-streaming velocity field in Plane 3, showing recirculating flow around the pMUT/cannula geometry; color scale, streaming speed.

(D) Interpolated velocity components (v_x for Plane 1; v_y for Plane 2) reconstructed from particle trajectories; color scale spans −600 to +600 μm/s, with characteristic dipolar lobes about the cannula tip. Scale bar, 300 μm.

(E) Line scan of particle velocity components v_x and v_y (in-flow vs. out-flow lanes) over distance, showing antisymmetric flow lanes consistent with acoustic streaming.

(F) Line scan of particle speed (in-flow and out-flow; measured vs. simulated) showing >100 μm/s flow sustained over hundreds of micrometers.

(G) Axial hydrophone pressure measurements in water, reported as peak-to-peak values, with individual measurements, experimental mean ± SD, and the simulated profile shown separately. The largest individual measurement approaches ~1 MPa at the closest sampled positions (nominal distances <50 μm); the scan extends to ~250 μm. Distances are based on micromanipulator positioning. See also Figure S6; Video S1.

phantom, defined as the maximum force between 50 and 100 s, and the insertion force at the end of the insertion phase, measured at t = 200 s.

During the puncturing phase, LUCID did not require a significantly different peak force than the Hamilton syringe control (Figure S7), with the peak puncturing force of LUCID totaling 12.74 ± 9.35 mN and the peak puncturing force of the control being 7.33 ± 2.53 mN, (p = 0.0588, unpaired two-sided Student's t test). This is important because the device geometry and material compliance differ substantially from a rigid metal syringe, yet these design differences did not translate into a significant penalty during the initial puncture. In contrast, at the end of insertion, LUCID exhibited a significantly lower insertion force than the syringe control (final insertion force of LUCID, 14.57 ± 18.57 mN; final insertion force of Control, 36.1 mN ± 17.35 mN, p = 0.00199). This 2.48-fold reduced force at full insertion suggests that, after tissue entry, LUCID imposes less-sustained mechanical loading on the surrounding phantom than the rigid syringe, which can be supported by the engineered geometry of the two-photon-printed polymer cannula tip and the compliance

Please cite this article in press as: Hou et al., Long-term ultrasound-enhanced convective injection device for neural drug delivery, Device (2026), https://doi.org/10.1016/j.device.2026.101333

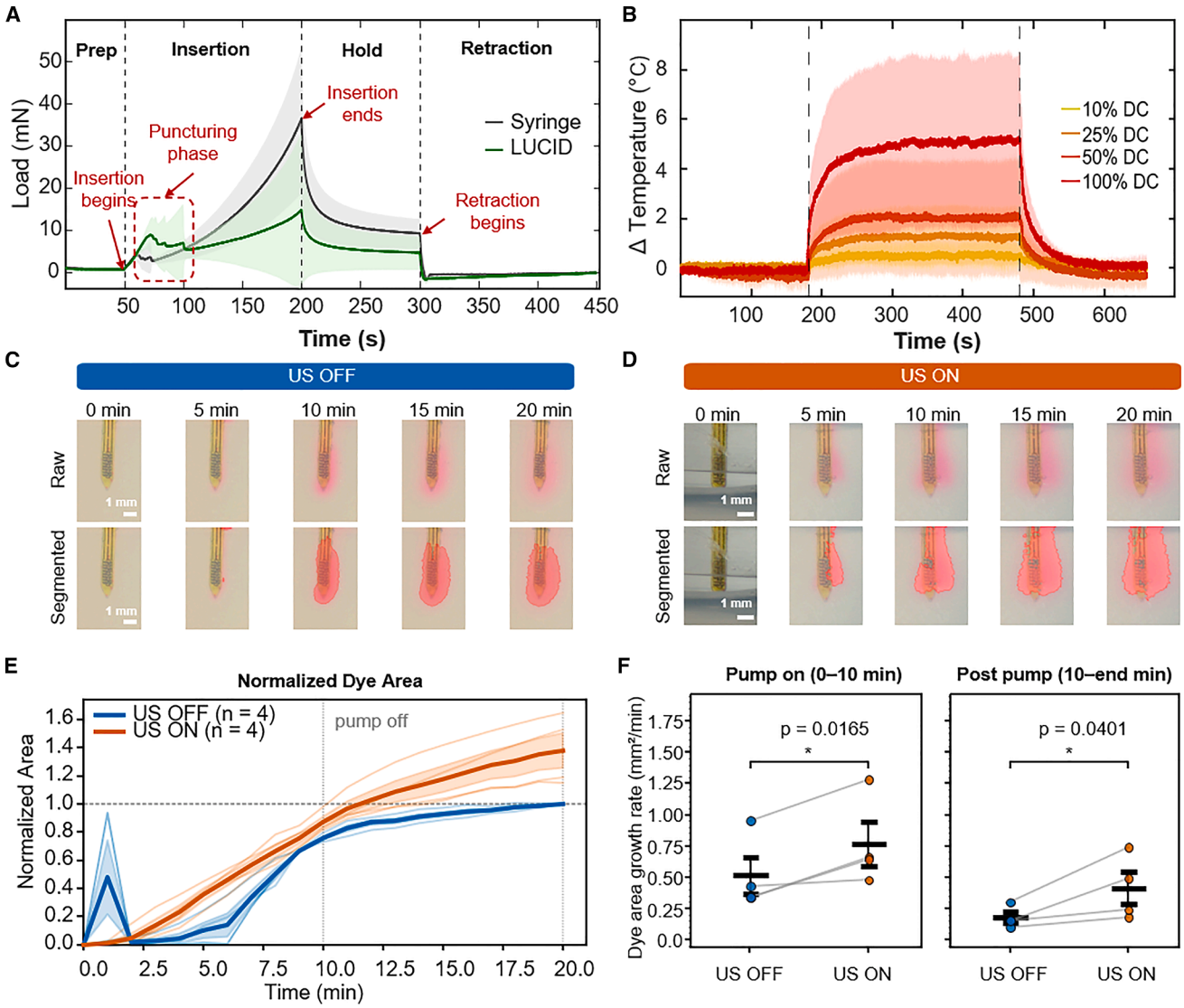


Figure 4. Mechanical insertion thermal response and acute phantom delivery

(A) Force-time profile of LUCID and a 26-gauge 30°-beveled Hamilton #701 syringe (Control) inserted into a 0.6% agarose brain phantom on an Instron 4411 with a 5-N load cell. The four phases are highlighted: prep, insertion, hold, and retraction. End-of-insertion (t = 200 s) force was 14.57 ± 18.57 mN for LUCID and 36.1 ± 17.35 mN for the syringe (n = 24 LUCID runs across 4 phantoms, n = 12 syringe controls).

(B) Thermal characterization with the device driven at resonance with a 10-V_{pp} sinusoid, pulse-repetition frequency 1 kHz, and varying duty cycle (10%, 25%, 50%, 100%). Temperature change (ΔT) was recorded with a Type-K thermocouple ~1 mm above the device, while the device and sensor were submerged in room temperature water; baseline 3 min OFF, 5 min ON, 3 min OFF post-stimulation. Average maximum ΔT (mean ± SD across 3 devices): 0.84°C ± 0.35°C (10% DC), 1.53°C ± 1.01°C (25% DC), 2.67°C ± 2.03°C (50% DC), and 5.67°C ± 3.58°C (100% DC).

(C) Time-lapse of rhodamine B infusion into a 0.6% agarose phantom with ultrasound OFF, at t = 0, 5, 10, 15, and 20 min (pump on 0–10 min; post-pump 10–20 min). Upper row, raw bright-field frames; lower row, the same frames with the segmented dye region overlaid. Scale bar, 1 mm

(D) The matched US-ON condition for the same device, with identical time points and row organization. Scale bar, 1 mm.

(E) Normalized dye-area trajectories over 0–20 min (pump on, 0–10 min; post-pump, 10–20 min). Mean ± SD across n = 4 devices; individual device traces are overlaid in light color.

(F) Dye-area growth rates during pump activation ± SD (left) and the post-pump phase ± SD (right), in mm^2/min. Lines connect matched US-OFF and US-ON runs from the same device (n = 4 device pairs). Paired two-sided t tests: p = 0.0165 during pump activation and p = 0.0401 after pump cessation.

See also Figures S5, S7–S11, and S15; Tables S2 and S3; and Notes S1 and S2. Shaded bands in (A) and (B) represent mean ± SD across the indicated runs or devices.

of the flexible device. For a chronic implantable device, this distinction is critical: the initial puncture force determines whether the device can be placed without excessive insertion trauma, whereas the end-of-insertion force better reflects the mechanical burden that may persist at the implant-tissue interface.

Please cite this article in press as: Hou et al., Long-term ultrasound-enhanced convective injection device for neural drug delivery, Device (2026), https://doi.org/10.1016/j.device.2026.101333

To confirm that this compliance does not come at the expense of insertability, we assessed through simulations whether either device approached its mechanical stability limit during entry. We estimated the critical buckling force of the LUCID insertion shaft and of the 26-gauge Hamilton needle both analytically, using Euler's column formula (Note S1), and numerically, using finite-element linear buckling analysis (COMSOL Multiphysics 6.1, Table S2), under the most conservative boundary condition, which corresponds to when the proximal end fixed at the fixture (the end of the Kapton tape for LUCID and the needle-barrel junction for the syringe) and the distal tip free (Figure S8, LUCID; Figure S9, syringe). Treating the LUCID shaft as a hollow-rectangular UpPhoto beam gave a critical force of 53 mN, with close agreement between the closed-form estimate and the finite-element solution (critical load factor λ = 4.24 at a 12.74 mN reference load). The equivalent analysis of the borosilicate and 304 stainless-steel Hamilton needle gave 375 mN and 377 mN numerically (λ = 51.37 at a 7.33 mN reference load). Both devices, therefore, operate well below their buckling thresholds: LUCID by roughly 4-fold relative to its own peak puncturing force and the syringe by roughly 51-fold; thus, LUCID's flexibility does not compromise its insertability. Notably, LUCID satisfies this stability requirement while using a lower-modulus material and a smaller cross-sectional footprint than the rigid metal syringe, the combination that minimizes tissue displacement and chronic mechanical mismatch at the implant-tissue interface.

Together, these results support LUCID as mechanically suitable for implantation, combining puncture forces comparable to a standard syringe with significantly reduced force after insertion. Furthermore, LUCID's flexible polymer body[46] and encapsulation with SU-8, which has been reported as biocompatible in neural tissue,[51] contribute to minimizing chronic mechanical mismatch and tissue irritation at the implant-tissue interface, thus supporting atraumatic insertion as well as chronic biocompatibility relative to rigid metal probes.[52]

Thermal characterization of LUCID at different duty cycles (Figure 4B) assessed heating during repeated actuation at 10 V_{pp}. Although there are no official regulatory mandates that explicitly specify a temperature increase limit for neural tissue in US applications, the International Transcranial Ultrasonic Stimulation Safety and Standards consortium (ITRUSST) presented in consensus recommendations of thermal parameters in transcranial US uses.[53] If any of the criteria defined by ITRUSST is met, the application is considered a "non-significant risk." We recognize our application is related neither to transcranial US nor to neuromodulation, but we have adopted these conservative thermal usage thresholds as our device operates in the brain and demonstrated that, through application of different duty cycles, the thermal effects of LUCID can be modulated.

Devices were submerged in DI water and driven at resonance with 10 V_{pp}, pulse repetition frequency (PRF) 1 kHz, and varying duty cycle (10%, 25%, 50%, 100%), with a Type-K thermocouple (Evolution Sensors and Controls, USA) positioned ~1 mm above the array. Temperature traces reached steady state within minutes of US-ON and recovered to baseline upon US-OFF; the average maximum ΔT scaled monotonically with duty cycle (Figure S10).

Only the 10% and 25% duty cycles (ΔT = 0.84°C ± 0.35°C and 1.53°C ± 1.01°C) produced thermal rises within ITRUSST's primary $\leq$2°C peak bound for non-significant risk.[53] At 50% and 100% DC (ΔT = 2.67°C ± 2.03°C and 5.67°C ± 3.58°C), peak ΔT exceeded 2°C; the alternative ITRUSST thermal-dose criterion (CEM43 $\leq$ 2)[53] was assessed using the CEM43 formulation[54]: ~3.4 h at 50% DC and ~3.2 min at 100% DC (Note S2). These duty cycles thus enable hours-long operation at 10%–50% DC (>3–43 h to reach 2 CEM43) and minutes-long operation at 100% DC while remaining within non-significant risk consensus. For therapeutic hypothermia applications (e.g., in tumors), even higher/longer exposures could be justified if blood flow is accounted for and clinical benefit outweigh risks, though this exceeds ITRUSST's conservative estimates. These results constrain chronic submerged-water bench operation to $\leq$25% DC for the $\leq$2°C criterion alone but motivate *in vivo* validation where cerebral perfusion dramatically expands the safe envelope. Crucially, the dye-enhancement effect demonstrated below is achieved within this safe duty-cycle range, which motivates direct *in vivo* thermal measurement, where convective heat removal by cerebral blood flow is expected to enlarge the safe operating envelope.

The measured water-tank pressures of ~0.8 MPa (Figure 2G) and up to ~1 MPa (Figure 3G) are peak-to-peak values, p_{pp}. Under an approximately symmetric sinusoidal-waveform assumption, $p_r \approx p_{pp}/2$ gives peak rarefactional amplitudes of ~0.40 and ~0.50 MPa. At 300 kHz, the corresponding non-derated water-based MI estimates, $p_r/\sqrt{f}$ (p_r in MPa; f in MHz), are ~0.73 and ~0.91. Both nominal estimates are below the 1.9 benchmark discussed in FDA diagnostic-US guidance and ITRUSST recommendations.[53,55] These water-based estimates use the stated waveform approximation and do not establish *in situ* brain exposure or device safety.

Under a sinusoidal traveling-wave approximation, $I \approx p_{pp}^2/(8\rho c)$ gives pulse-average intensity estimates of ~5 and ~8 W/cm^2, respectively, using brain properties (ρ = 1,040 kg m^{-3} and c = 1,560 m s^{-1}[43]). These are pressure-based estimates; near-field intensity, duty cycle, exposure duration, and heating require separate assessment. The device is also built from materials with established neural biocompatibility: its SU-8 surface and KNN/Cr-Au transducer stack supported cortical-neuron viability over 10 days *in vitro* and showed minimal GFAP$^+$ astrogliosis at 14 days post-implantation in a prior device from our group,[30] SU-8 is independently validated for long-term neural probes,[51,56] and the UpPhoto resin used for the microfluidic channels has passed ISO 10993-5 cytotoxicity testing.[57]

We then investigated whether the active acoustic streaming demonstrated in Figure 3 translates into actionable enhancement of payload distribution in tissue-like media. Rhodamine B was infused into 0.6% agarose brain phantoms by a syringe pump attached to LUCID via a silicone tube under matched conditions (Figure S11), with US either off (control) or on at the device resonance (Figures 4C–4F). The LUCID transducer array was driven at the device's resonance frequency with 10 V_{pp} amplitude, 25% duty cycle, and 1 kHz pulse-repetition frequency. Time-lapse imaging over 0–20 min showed larger dye-distribution patterns with US-ON (Figure 4D) than with US-OFF

Please cite this article in press as: Hou et al., Long-term ultrasound-enhanced convective injection device for neural drug delivery, Device (2026), https://doi.org/10.1016/j.device.2026.101333

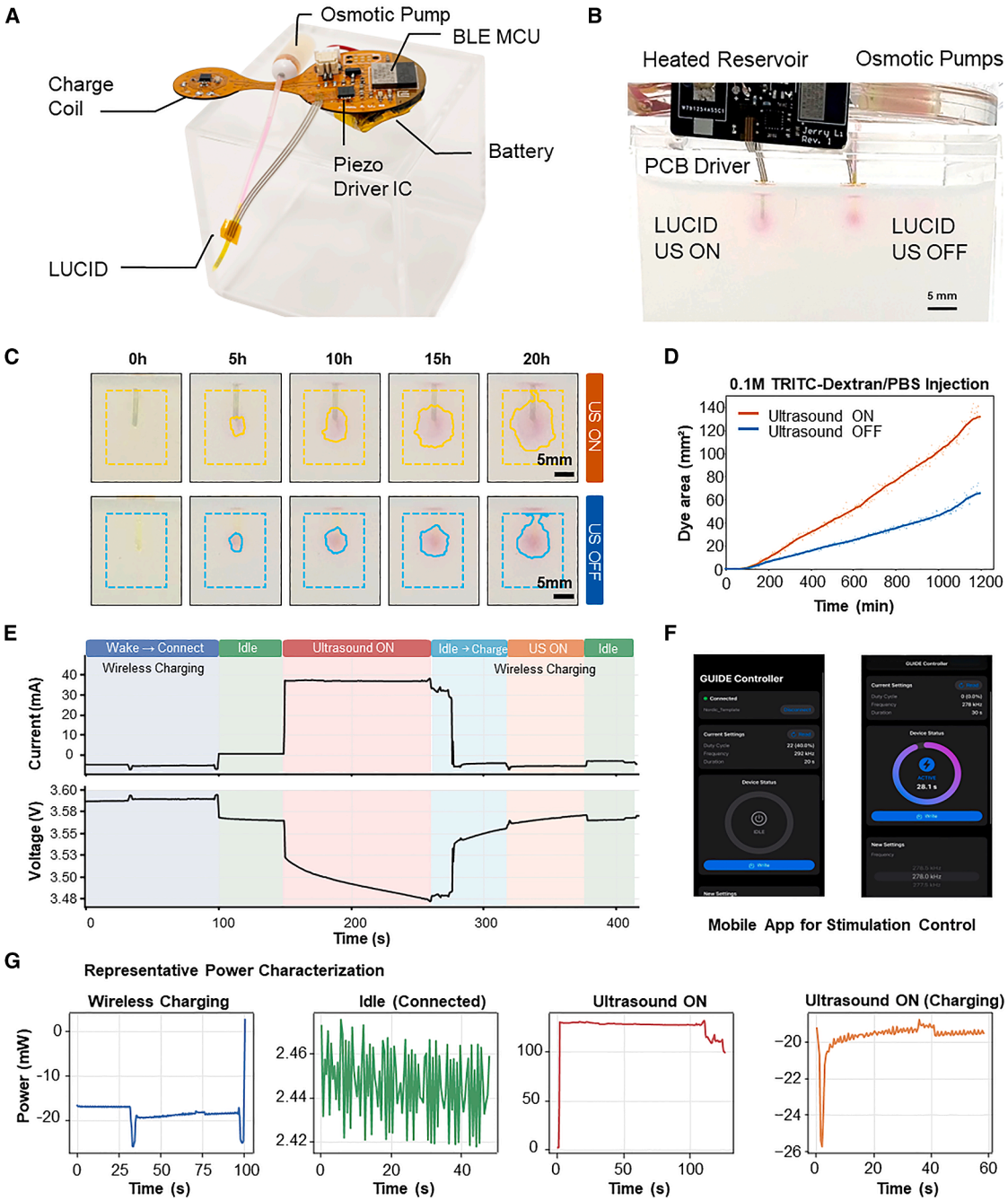


Figure 5. Wireless operation and long-duration phantom delivery

(A) Photograph of the integrated LUCID system: pMUT array, microfluidic cannula, custom PCB with NRF52840 SIP, BLE service, integrated boost + piezo driver, charge coil, Li-ion battery, and two osmotic pumps mounted in a heated reservoir.

(B) Diagram of the experimental setup for chronic dye infusion with 1 μM TRITC-dextran. Two devices (US-ON, left) and (US-OFF, right) inserted into the same 0.6% agarose neural tissue phantom. Osmotic pumps submerged in water at 37°C with silicone tube feedthroughs into the tissue phantom prevent leakage. The wireless drive PCB is mounted outside the chamber in air. Scale bar, 5 mm.

(C) Time-lapse images from a representative long-duration *in vitro* phantom delivery experiment (0–20 h), with the device operated wirelessly throughout and an integrated osmotic pump providing continuous infusion. Snapshots at matched time points (5, 10, 15, 20 h) show progressively larger TRITC-dextran distribution under US-ON (top row) vs. US-OFF (bottom row). Scale bar, 5 mm.

(D) Cumulative dye area over the full 20-h experiment, US-ON (red) vs. US-OFF (blue). Linear-fit growth rate (full 20-h window): 6.87 ± 0.10 mm^2/h under US-ON (R^2 = 0.983) vs. 3.21 ± 0.06 mm^2/h under US-OFF (R^2 = 0.974): a 114% higher rate (~2.1×) under US-ON. Endpoint dye-distribution area (mean of the last 10

(legend continued on next page)

Please cite this article in press as: Hou et al., Long-term ultrasound-enhanced convective injection device for neural drug delivery, Device (2026), https://doi.org/10.1016/j.device.2026.101333

(Figure 4C), with the pump active during 0–10 min. Normalized dye-area trajectories are shown in Figure 4E. Dye-area growth rates were higher under US-ON during both pump activation and the post-pump phase (Figure 4F; paired two-sided *t* tests, $p = 0.0165$ and $p = 0.0401$, respectively; $n = 4$ paired US-ON/US-OFF runs on $n = 4$ devices). The persistence of enhancement after the pump turns off indicates that the acoustic field reshapes the local interstitial transport state rather than acting only as a transient flow driver, which is an important property for any chronic delivery regimen in which the pump duty cycle is decoupled from the US duty cycle.

Fully wireless operation enables long-duration *in vitro* delivery

The complete LUCID system integrates the validated pMUT array and microfluidic cannula with a passive osmotic-pump reservoir and a custom wirelessly powered drive PCB (Figures 5A and 5B; component-level photographs and inductive-charging waveforms in Figure S12). The PCB centers on a Bluetooth Low Energy SIP (Nordic NRF52840) controlling an integrated boost converter and piezo driver that supplies the array with the resonant 10-V drive used in the bench characterization with a controllable frequency with 5 kHz resolution between 20 and 500 kHz. Power is supplied either by an on-board Li-ion cell or, transiently, directly from a resonant inductive coil during charging (Figure 5B), allowing the device to be operated and recharged through intact tissue without external connections.

We performed a long-duration *in vitro* phantom delivery experiment (Figures 5C and 5D, Video S2; experimental setup in Figure S13) with the device operated wirelessly throughout and an integrated osmotic pump providing continuous infusion. Across 0–20 h of operation, US-ON consistently produced larger dye-distribution areas than matched US-OFF devices (Figure 5C). A linear fit to the full 20-h growth curve (Figure 5D) gave a slope of 6.87 ± 0.10 mm^2/h under US-ON ($R^2 = 0.983$) vs. 3.21 ± 0.06 mm^2/h under US-OFF ($R^2 = 0.974$), corresponding to a 114% higher growth rate, approximately 2.1×, under US-ON. The endpoint dye-distribution area (mean of the last 10 samples) reached 135.8 mm^2 under US-ON vs. 67.5 mm^2 under US-OFF, with US-ON roughly twice as large. This long-duration comparison reflects a single paired US-ON/US-OFF run ($n = 1$ device pair); thus the high R^2 values (0.983, 0.974) describe the internal consistency of the 20-h growth curve's repeated time sampling within that single run, not device-to-device reproducibility. The linear scaling of both curves over the full 20-h window indicates that the US-mediated enhancement is sustained across the full 20-h observation window rather than acting only transiently.

We quantified within-bolus uniformity from the segmented contrast region (coefficient of variation [CV] = σ/μ of signal intensity across the bolus, and the center-to-edge intensity ratio; Figure S14). Under LUCID operation, the bolus was measurably more uniform than the passive control (CV = 0.335 vs. 0.360; a ∼7% reduction sustained across the imaging window), while both profiles retained a graded, Gaussian-like radial decay rather than a fully convective top-hat, consistent with the intermediate Péclet regime quantified below.

Wireless operation was validated in three complementary ways. First, the BLE/charging firmware implements a state machine (Figure 5E) that cycles between idle, wake-on-connect, US-ON, and wireless-charging states, exposing a high-level service that allows arbitrary infusion regimens to be triggered and monitored from a paired mobile device. Second, power analyzer measurements of supply current, battery voltage, and instantaneous power across each phase (Figure 5E) showed clean transitions between modes with no measurable drift in stimulation current when US was operated simultaneously with active wireless charging. These states are controlled by a custom mobile application that includes an interface for programming and tracking stimulation protocols (Figure 5F). Per-phase means from the trailing 60% of each operating phase (Figures 5G and S12) were 0.69 mA at 3.57 V (2.45 mW) during BLE-connected idle, 36.89 mA at 3.49 V (128.6 mW) during US operation without charging, −5.22 mA (−18.74 mW) during charging only, and −5.53 mA (−19.73 mW) during simultaneous US operation and charging. Negative values indicate net battery charging. These measurements characterize operating current and do not establish standby duration. The cell's nominal rating was 3.7 V/110 mAh; the measured battery voltage ranged from 3.49 to 3.59 V across these phases.

Together, these results provide a proof-of-concept demonstration that the integrated LUCID system can operate without tethered electrical connections for a continuous 20-h delivery window, with payload throughput modulated by on-device US. While true chronic *in vivo* dwell times have yet to be characterized, this 20-h wireless *in vitro* operation provides the technical basis for the longitudinal regimens motivated in the "introduction" section.

In vivo MRI demonstrates enhanced parenchymal distribution and tumor delivery

We next tested whether the *in vitro* enhancement transferred to brain tissue. Adult male C57BL/6 mice received an intracortical infusion of gadobutrol contrast agent (Gadavist, 2 μL of a 1:100 saline dilution at 0.2 μL/min over 10 min, with a 10-min post-infusion dwell) at AP +0.5 mm, ML +1.5 mm, DV −3.0 mm from bregma, delivered through either a 26-gauge Hamilton #701 syringe (CED control) or an implanted LUCID cannula with US-ON

samples, to dampen single-frame noise): 135.8 mm^2 (US-ON) vs. 67.5 mm^2 (US-OFF), with US-ON ∼2-fold larger (last-sample values 130.8 vs. 66.1 mm^2; peak observed 142.6 vs. 74.0 mm^2).

(E) State diagram with time-dependent trace of the BLE/charging firmware: idle, wake/connect, ultrasound ON, idle/charge, and wireless-charging cycle.

(F) Screenshots of the user interface on the mobile application used for wireless control of the ultrasound actuation protocol.

(G) Per-phase mean voltage (V), current (I), and power (P) computed over the trailing 60% of each labeled phase in the I, V, and P trace in (E): wireless charging only (V = 3.589 V, I = −5.22 mA, P = −18.74 mW), idle while BLE-connected (V = 3.565 V, I = 0.69 mA, P = 2.45 mW), ultrasound ON without charging (V = 3.486 V, I = 36.89 mA, P = 128.62 mW), and ultrasound ON during simultaneous wireless charging (V = 3.566 V, I = −5.53 mA, P = −19.73 mW). Negative current/power values denote net energy flow into the battery during charging; positive values denote net discharge during ultrasound operation. See also Figures S12–S15 and Table S3. The chronic experiment used one US-ON/US-OFF device pair; slope uncertainties are 95% confidence-interval half-widths.

Please cite this article in press as: Hou et al., Long-term ultrasound-enhanced convective injection device for neural drug delivery, Device (2026), https://doi.org/10.1016/j.device.2026.101333

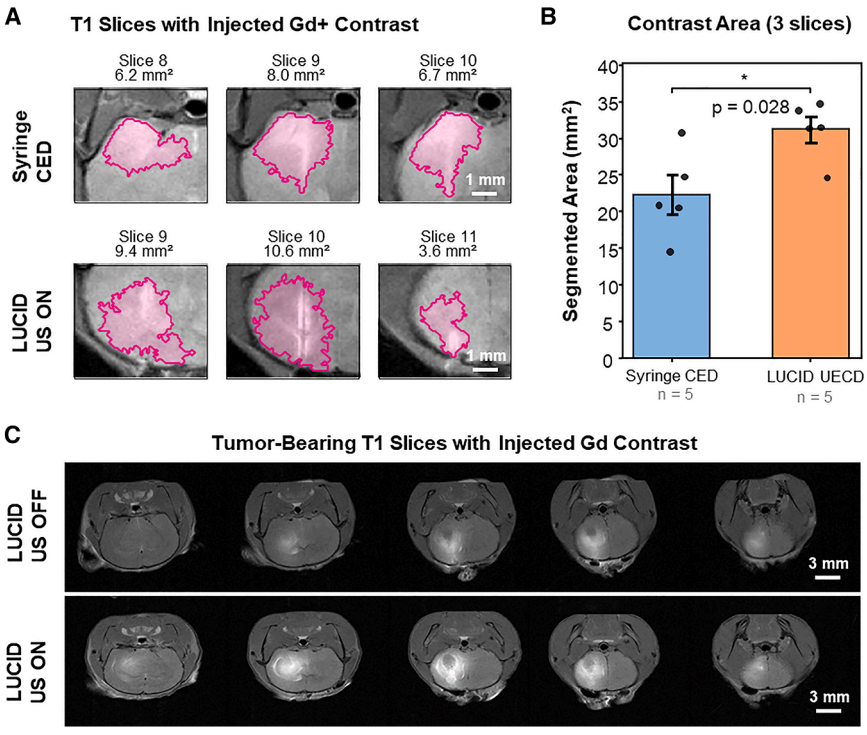


Figure 6. Acute intracortical contrast distribution in mouse brain

(A) Illustrative T1-weighted MRI slices acquired ~1 h after intracortical infusion of gadobutrol contrast (Gadavist; 2 μL at 0.2 μL/min over 10 min, with a 10-min post-infusion dwell during which ultrasound was applied for the LUCID arm at 10 V_{pp}, 30% duty cycle, at the device resonance frequency [300–400 kHz]) in a naive adult male C57BL/6 mouse brain, comparing Hamilton-syringe CED (top row) and LUCID UECD with US-ON (bottom row), shown across three contiguous coronal slices per subject centered on the injection site (AP +0.5, ML +1.5, DV −3.0 from bregma). Because gadobutrol does not cross the intact blood-brain barrier, the contrast distribution shown reflects direct intracortical delivery and interstitial transport. Per-slice contrast-enhanced areas: syringe 6.2/8.0/6.7 mm^2 and LUCID 9.4/10.6/3.6 mm^2 for the illustrated subjects. (A) One subject per condition for illustration; cohort statistics are presented in (B). Scale bars, 1 mm.

(B) Total contrast-enhanced volume (mm^3) per subject, summed across the three labeled slices. Group means (mean ± SD): syringe CED 22.3 ± 6.0 mm^3 (n = 5), LUCID UECD 31.2 ± 4.3 mm^3 (n = 5); unpaired two-sided t test, p = 0.028.

(C) Representative tumor-bearing T1-weighted slices (n = 1) comparing LUCID with US-OFF and US-ON in a CT-2A/fLuc syngeneic glioma model (50,000 cells inoculated 7 days prior at the same coordinates). The contrast agent appears more concentrated and broadly distributed throughout the tumor volume under US-ON than under US-OFF; given the single-subject sample size, this case is shown for illustrative purposes only, and no statistical comparison is drawn. Scale bars, 3 mm.

See also Figures S15–S17, Table S3, and Note S3.

(US-enhanced convective delivery [UECD]; 10 V_{pp} at the device resonance frequency between 300 and 400 kHz, 30% duty cycle, applied for the 10-min post-infusion dwell only). Because gadobutrol does not cross the intact BBB, the contrast distribution observed reflects direct intracortical delivery and subsequent interstitial transport rather than vascular uptake, a deliberate design choice that isolates the mechanical/convective enhancement provided by acoustic streaming from any BBB-disrupting effect of the US.

Mice were imaged ~1 h after the end of infusion on a 3 T Bruker BioSpec scanner using a T1-weighted RARE sequence (TR/TE/RARE factor = 1,000/10 ms/2; matrix 192 × 192; FOV 20 × 17.17 mm; slice thickness 1 mm; 15 contiguous axial slices; full parameters in the methods section), and the gadolinium-enhanced volume was segmented across three contiguous coronal slices per animal.

In the subjects illustrated in Figure 6A, per-slice contrast-enhanced areas were 6.2/8.0/6.7 mm^2 for syringe CED and 9.4/10.6/3.6 mm^2 for LUCID UECD. Figure 6A shows one subject per condition for illustration; the cohort comparison follows. Within-bolus uniformity was not quantified *in vivo*. Across the full cohort (n = 5 per arm; Figure 6B), the total contrast-enhanced volume was 22.3 ± 6.0 mm^3 for syringe CED and 31.2 ± 4.3 mm^3 for LUCID UECD (mean ± SD; unpaired two-sided t test, p = 0.028), which represents an approximately 40% increase in the distribution volume at matched infusion volumes and rates.

To place the three delivery regimes evaluated in this study on a common physical axis, we computed Péclet numbers (Pe = advective transport/diffusive transport) for each. We report two complementary quantities: a pump-only Péclet number $Pe_{pump} = Q/(4\pi rD)$, which locates the nominal pump flow alone on the diffusion-convection axis, and an observed Péclet number $Pe_{obs} = \langle r \rangle \cdot (dr/dt)/D$ computed from the measured bolus front speed, which captures the combined effect of pump flow, diffusion, and acoustic streaming (Figure S15, Table S3). Across the acute *in vitro* (0.5 μL/min), chronic *in vitro* (1 μL/h), and *in vivo* (0.2 μL/min) regimes, Pe_{pump} spanned more than 10-fold during pump operation and straddled the Pe = 1 diffusion-convection boundary, confirming that these protocols occupy fundamentally different transport regimes (Figure S15A). In every regime, LUCID operation elevated Pe_{obs} above the passive control: the enhancement was largest where the passive baseline was diffusion-dominated (2.25-fold in the pump-off phase of the acute experiment; 1.34-fold in the chronic experiment) and smaller where pump-driven convection was already established (1.46-fold in the pump-on phase). *In vivo*, LUCID produced a 1.26-fold increase in Pe_{obs} over the passive-needle control (Pe_{obs} = 3.53 ± 0.14 vs. 2.81 ± 0.23, mean ± SEM, n = 5 per group; Welch's t test p = 0.031), providing a transport-regime interpretation of the MRI volume comparison (pump-only Péclet number ≈0.96). The *in vivo* Péclet values derive from the same segmented MRI volumes used in Figure 6B and are not an independent measurement of transport.

Please cite this article in press as: Hou et al., Long-term ultrasound-enhanced convective injection device for neural drug delivery, Device (2026), https://doi.org/10.1016/j.device.2026.101333

To extend this from naive to pathological tissue, we performed an illustrative experiment in CT-2A/fLuc syngeneic glioma-bearing mice (50,000 cells inoculated into the right striatum at the same coordinates 7 days prior to imaging; Figure 6C). Comparing LUCID with US-OFF and US-ON within the same tumor model, the contrast agent appeared more concentrated and broadly distributed throughout the tumor volume under US-ON. Given the $n = 1$ sample per arm, this case is presented as illustrative only (see "discussion" section).

Together, these *in vivo* Gd-MRI results constitute the primary translational evidence that LUCID provides enlarged parenchymal distribution beyond conventional syringe CED at clinically relevant infusion volumes and rates, while operating through a chronically implantable, wirelessly powered platform.

Preliminary evidence on CD3/CD8 recruitment in a tumor-bearing model

Chronic, repeated delivery of US stimulation has been hypothesized to have an immunomodulatory effect, causing improved T cell response that can be harnessed in conjunction with immunotherapy.[22,58] To investigate the delayed effect of implantation and stimulation of LUCID, we conducted further experiments in a GBM mouse model (Figure S16). Using CD3 and CD8 immunohistochemistry on tumor-bearing sections ($n = 8$ mice per condition, both receiving identical device implantation and differing only in whether US was activated, with three anatomical regions quantified per animal: exterior cortex, exterior midline, and tumor core), we observed no consistent increase in cytotoxic ($CD3^+CD8^+$) T cell infiltration attributable to US exposure (Figure S17). $CD8^+$ counts showed a significant condition $\times$ region interaction ($F(2,42) = 7.30$, $p = 0.0019$), driven by lower counts under US-ON in the exterior cortex and midline but not in the tumor core; no individual region reached significance after correction for multiple comparisons. Experiment and analysis details can be found in the methods section and Note S3.

These findings remain preliminary, as sample sizes were limited, absolute $CD8^+$ counts were low, and the experiment was designed to assess CD3/CD8 infiltration only. They indicate that, under the exposure conditions and endpoints tested, US stimulation did not produce a detectable increase in T cell infiltration in this model. They neither address other components of the neuroinflammatory response, which could be assessed through microglial or astrocytic activation and cytokine signaling, nor do they exclude effects at other exposure parameters or time points. We report this exploratory result because it establishes an initial biological-response baseline for a distinct exposure modality, as LUCID generated US locally from an implanted source, without transcranial propagation, circulating microbubbles, or systemic therapeutic administration used in previous cancer immunotherapy studies.[22,58]

DISCUSSION

Three themes emerge from these results: UECD provides a quantifiable distribution advantage over pressure-driven infusion alone in both *in vitro* and *in vivo* models; the entire system can be miniaturized and chronically implanted while preserving acoustic performance; and the resulting platform fills a niche in CNS drug delivery that no existing technology individually occupies.

The physical basis of the distribution advantage is acoustic streaming at the cannula tip.[33,36] Hydrophone measurements in water show near-tip peak-to-peak pressures approaching $\sim$1 MPa at the closest sampled positions (Figure 3G), while particle tracking independently characterizes dipolar streaming velocities of $\pm$600 μm/s and sustained directional flow >100 μm/s over hundreds of micrometers (Figures 3D–3F)—magnitudes consistent with COMSOL simulation. The relative contributions of convection and diffusion are quantified in our Péclet analysis (Figure S15 and Table S3). Importantly, the *in vitro* dye-infusion experiments (Figures 4E and 4F) in a tissue-mimicking model show that the enhancement persists into the post-pump phase, suggesting that US could alter the local interstitial transport state rather than acting only as a transient flow driver. The long-duration osmotic-pump experiment (Figure 5D) extends this to a 20-h continuous-operation window in which the dye-area growth rate under US-ON (6.87 mm^2/h; $R^2 = 0.983$) was $\sim$2.1$\times$ that under US-OFF (3.21 mm^2/h; $R^2 = 0.974$) and showed no signs of saturation, demonstrating that the streaming-mediated enhancement is sustained across the full 20-h window, with no sign of saturation.

This distribution advantage can be framed quantitatively through the Péclet number, which sets the balance between advective and diffusive transport (Figure S15, Table S3). The three delivery regimes examined here span this balance almost completely: the acute *in vitro* syringe-pump protocol (0.5 μL/min) is already mildly convective on pump flow alone ($Pe_{pump} \approx 2.1$), whereas the chronic osmotic-pump protocol (1 μL/h) is strongly diffusion-dominated on pump flow alone ($Pe_{pump} \approx 0.19$) because the large, slowly diffusing dextran integrates only a small convective contribution per unit time. The *in vivo* contrast infusion (0.2 μL/min) sits almost exactly on the Pe = 1 boundary ($Pe_{pump} \approx 0.96$), placing it in the transport regime most sensitive to added convection. Against this backdrop, the observed Péclet numbers reveal a consistent pattern: acoustic streaming raises Pe_{obs} above the passive baseline in every regime, and the magnitude of enhancement scales inversely with how convective the baseline already is: a modest boost when the pump alone drives convection (1.46-fold) and a larger boost when diffusion dominates the baseline (up to 2.25-fold *in vitro*; 1.26-fold in the volume-derived *in vivo* analysis). This behavior indicates that LUCID does not simply amplify existing flow but can induce convective transport where passive delivery would otherwise be diffusion limited.

LUCID does not rely on US to cross the BBB: intraparenchymal infusion bypasses the barrier by construction. US is included to supply an active convective transport term at the cannula tip that is independent of pump pressure, and thereby to address the limitation that actually constrains CED, which is the distribution volume attainable at the low flow rates a chronic implanted reservoir must use. According to the Péclet analysis we performed, the streaming enhancement is the largest where pressure-driven convection is the weakest (2.25-fold when the baseline is diffusion dominated) and the smallest where the pump alone already drives convection (1.46-fold), which is the

Please cite this article in press as: Hou et al., Long-term ultrasound-enhanced convective injection device for neural drug delivery, Device (2026), https://doi.org/10.1016/j.device.2026.101333

signature of an added transport term rather than an amplification of existing flow.

A reasonable concern is that US-mediated barrier modulation might permit locally infused drugs to escape into the systemic circulation, reducing parenchymal retention. Within the delivered drugs in the *in vivo* study, gadobutrol is impermeant to the intact barrier in both directions, and the retained contrast-enhanced volume 1 hour after infusion was 40% larger under US ($p = 0.028$). Three considerations bound the concern mechanistically. First, convective flux is directed outward from the cannula into tissue; increased permeability raises bidirectional diffusive exchange but does not reverse the imposed pressure gradient. Second, LUCID operates without circulating microbubbles, the dominant mechanism of transcranial FUS-mediated barrier opening; sustained opening is not expected at these frequencies and pressures in the absence of cavitation nuclei. We regard this as a prospective advantage of the architecture rather than as a result of the present study, which was deliberately designed with a barrier-impermeant tracer to isolate the convective contribution.

Compared with the existing post-resection delivery technologies surveyed in the "introduction" section, LUCID occupies a distinct position. Carmustine wafers and polymer/hydrogel matrices[6,8] provide passive sustained release but cannot be modulated after implantation and have limited diffusion ranges. Catheter-based CED[12] achieves large-volume distribution but commonly relies on percutaneous catheters and external pumps. Locoregional CAR-T delivery[10] is another catheter-based approach. Tumor treating fields[11] provides chronic, programmable physical therapy but does not directly deliver biologics. Implanted systems such as MiNDS[40] have demonstrated chronic, programmable parenchymal delivery without active flow enhancement. The closest analog among injection-based US-enhanced delivery devices, the recently reported PULSE platform[35] relies on lead-containing bulk PZT-5A transducers necessarily tethered to bulky bench-top equipment including an RF power amplifier, in contrast to LUCID's lead-free, soft materials-based pMUT array integrated into a miniaturized form factor and that can be operated wirelessly. LUCID combines the active distribution enhancement of CED with the chronic implantability and wireless control of MiNDS-class devices and adds an integrated osmotic reservoir whose capacity (100 μL at a nominal 1 μL h^{-1}) is sufficient for several days of continuous infusion, although operation beyond 20 h has not been demonstrated.

Key technical contributions enabling this combination include (1) the use of biocompatible KNN as the piezoelectric, which avoids the lead and chemically active interfaces of conventional PZT and is an essential prerequisite for chronic implantation[30]; (2) the *in situ* two-photon-printed microfluidic cannula, which preserves sub-micrometer registration to the array and would be impractical to assemble post-fabrication[59]; (3) full integration of BLE control and resonant-inductive charging on a custom PCB, enabling simultaneous US operation and wireless charging without measurable drift in drive current (Figure 5E); and (4) a passive osmotic pump reservoir[60] that decouples payload throughput from electrical power demand, allowing the duty cycle of the US to be optimized independently of the infusion timeline.

Several considerations bear on translation. First, the thermal data (Figure 4B) constrain the chronic operating envelope: only the 10% and 25% duty cycles ($\Delta T = 0.84°C$ and $1.53°C$, respectively) fall within the conservatively accepted $\leq 2°C$ window for neural implants in our submerged-water configuration, allowing for chronic use without restrictions, while 50% and 100% DC exceed the bound (2.67°C and 5.67°C) and would have to act within the constraints of total treatment time to satisfy the low cumulative thermal dose requirement. *In vivo* thermal behavior in perfused tissue is expected to be more favorable due to convective heat removal by cerebral blood flow, but chronic safety windows under realistic operating profiles remain to be measured directly; in the meantime, chronic operation should default to $\leq$25% DC. Second, the *in vivo* cohort here was naive, acutely infused, and confined to a single rodent strain (C57BL/6); generalization to larger species, additional brain regions, and tumor-bearing brains will require dedicated study. Establishing chronic tolerability is a prerequisite for the intended use case of sustained, repeated intraparenchymal delivery and constitutes the natural next step. We, therefore, plan a chronic, awake-behaving study pairing US-ON and US-OFF implants, with GFAP and Iba1 immunohistology at multiple post-implantation time points to quantify astrogliosis and microglial activation, alongside neuronal-viability and device-dwell-time assessment under the repeated-stimulation regimen a drug-delivery application would require. Third, the tumor case shown in Figure 6C is a single illustrative subject and motivates rather than establishes efficacy in glioma; an expanded cohort using the CT-2A/fLuc model is the natural next step. In a related exploratory investigation in a tumor-bearing cohort, CD3/CD8 immunohistochemistry across the cortex, midline, and tumor-core regions found no evidence of a robust US-driven pro-inflammatory or cytotoxic T cell response (Figures S16 and S17). Focused-US exposure, particularly in combination with microbubble-mediated barrier disruption, has been reported to act as an immunomodulatory adjuvant in glioma models and to improve responses to checkpoint blockade[22,58]; whether pairing LUCID stimulation with such synergistic strategies can elicit a more pronounced pro-inflammatory shift remains an open question for future study.

Charging is performed transcutaneously by bringing an external transmitter (TX) coil adjacent to the implant site; at a TX-RX separation on the order of 5–15 mm (set by scalp thickness and coil placement), the resonant-inductive link operates within the LTC4124's input range and alignment tolerance. Because the LTC4124 manages rectification and the constant-current/constant-voltage charge profile entirely on the receive side, the link requires no primary-side feedback and is tolerant to modest coil misalignment, and the device's built-in low-battery disconnect and NTC temperature qualification enforce safe-charging limits if a session is interrupted. The on-board battery capacity substantially exceeds the energy required to exhaust the passive-reservoir fluid volumes used here, so rechargeability is provided to support future chronic regimens spanning weeks to months rather than to sustain the experiments reported in this study. The reliability of simultaneous operation and charging through this link is quantified in Figures 5E–5G: the battery received net energy even during concurrent US output, supply voltage remained within the Li-ion safe window,

Please cite this article in press as: Hou et al., Long-term ultrasound-enhanced convective injection device for neural drug delivery, Device (2026), https://doi.org/10.1016/j.device.2026.101333

and the device operated continuously under wireless power for 20 h. This behavior is consistent with published precedent for wireless powering and recharging of implantable devices.[61–64]

Looking forward, the same architecture supports payload classes well beyond the contrast agents tested here. The two-photon-printed cannula geometry is biocompatible and can be readily reprinted for larger-bore biologic delivery; the osmotic reservoir can be loaded with chemotherapeutics, viral vectors, or cell suspensions of compatible viscosity, and the BLE service exposes arbitrary stimulation regimens that can be programmed to match clinical or experimental dosing schedules. By providing a single platform that integrates active flow enhancement, programmable wireless control, and chronic implantability, LUCID expands the design space for direct intraparenchymal therapy in oncology, neurodegenerative disease, and circuit-level neuroscience.

The chronic-delivery capability of LUCID is supported here by *in vitro* phantom experiments only (Figures 5C and 5D, 0–20 h continuous wireless operation); *in vivo* demonstrations of distribution were limited to acute Gd-MRI immediately following infusion. A full demonstration of chronic utility: implantation with autonomous wireless operation and repeated dosing in awake, behaving animals, together with longitudinal imaging of distribution and endpoint histology of the implant-tissue interface is the direct next step for this platform and is the subject of a dedicated follow-on study. The *in vivo* MRI cohort was performed in a single mouse strain (C57BL/6) and used a single injection trajectory; generalization across larger species, brain regions, and disease models has yet to be established. The tumor-bearing data shown in Figure 6C are illustrative ($n = 1$) and motivate, but do not establish, efficacy in glioma-bearing brains. Finally, US parameters were chosen to maximize streaming and minimize heating in our phantom and acute settings; long-duration safety windows under realistic chronic duty cycles will require dedicated study. Additional limitations and translational considerations are discussed in Note S4.

METHODS

Additional analytical details and simulation parameters are provided in Notes S1–S4 and Tables S1–S3.

Implantation force

Realistic brain tissue phantoms were created, with 0.6% agarose gel, as described in Chen et al. 2004.[50] Agarose powder was mixed with 1× TBE and DI water, stirred and heated until boiling, and then cooled for 5 min before being poured into 30-mm diameter petri dishes. An Instron 4411 Tensile Tester with a 5-N load cell was used as a test frame for measuring the compressive and tensile forces of LUCID devices in comparison with Hamilton syringe #701 (Control). After mounting the device (LUCID or Control) to the Intron test frame, the operator would visually lower the device to be as close as possible, without touching the surface of the brain phantom, then the test frame was tared, and the displacement was zeroed. The displacement-controlled test consisted of a pre-test descent of the device until 1 mN compression was detected, followed by a 50-s hold that started the data acquisition. After the hold, the device is inserted into the phantom by 5 mm (speed 2 mm/min), allowed to rest for 100 s inside the phantom, and then retracted by 5 mm (speed 2 mm/min). Four brain phantom samples were tested, and for each sample, two LUCID devices and one control device were inserted into three different locations, totaling 24 device runs and 12 control runs.

Heating and thermal characterization

Three LUCID devices were driven by a function generator (Agilent HP 33120A) with a pure sinusoidal 10-V peak-to-peak signal at their resonant frequency (~300 kHz), with varying duty cycle (10%, 25%, 50%, and 100%) and constant PRF of 1 kHz. A thermocouple (Type K, Evolution Sensors) was placed above the device using a microscope, and both the sensor and the device were submerged in water (room temperature). The thermocouple temperature measurement was captured (DataQ Instruments DI-245) at baseline (device OFF) for 3 min, 5 min with device ON, and then 3 min after the device was turned OFF again.

pMUT array microfabrication

The fabrication of a similar single pMUT structure, based on KNN as the piezoelectric thin film and SU-8 as the structural material for the flexural membrane and air cavity, was demonstrated previously.[30] The LUCID device incorporates a multi-element pMUT array, with 24 elements arranged in parallel, where individual top and bottom electrodes are subsequently connected along the electrical traces. All photolithography iron oxide masks were designed with AutoCAD and fabricated with the Heidelberg Maskless Aligner MLA 150. The microfabrication took place in the YellowBox from the Conformable Decoders Group at MIT Media Lab and at mit.Nano.

The pMUT array is fabricated using a top-down approach, starting from the electrode-piezoelectric-electrode stack and moving on to the cavity structure. The initial substrate is a thin-film stack of 500 nm SiO_2, 610 μm Si, 500 nm SiO_2, 30 nm ZnO, 200 nm Pt, 1 μm KNN, 10 nm Cr, 150 nm Au (SCIOCS Co. Ltd., Sumitomo Chemical Group, JAPAN). The wafers were cleaved into approximately 20 × 20-mm squares, treated with hexamethyldisilazane (HMDS) adhesion promoter, and subsequently spin-coated with positive I-line photoresist (PR) (Microchemicals AZ4620) at a thickness between 10 and 15 μm to define the top electrode and piezoelectric layer. Each square held patterns for 16 devices. After contact photolithography (Karl Suss MJB4) exposure and development, the Au and Cr layers were wet etched using gold and CR-7 etchant (Transene), and the KNN layer was wet etched with a 49% hydrofluoric acid (HF, JT Baker) solution with agitation. Subsequently, the PR was stripped by submerging the wafer in an N-methyl-2-pyrrolidone (NMP) stripper solution (Microchem AZ400T) heated to 120°C and bringing the solution to an ultrasonic water bath for 5 min. The wafer then underwent another round of HMDS and PR (AZ4620) patterning for definition of the bottom electrode. The ZnO and Pt layers were dry etched using a reactive-ion etching (RIE) (Plasma-Therm VISION 320 RIE) recipe flowing Ar/O_2 at 95%/5% concentrations and power of 500 W. The final steps before transfer printing of the piezoelectric/electrodes stacks consisted of patterning of an anchor layer using HMDS and PR (AZ4620), and subsequent wet etching—using a 3:4 solution of

Please cite this article in press as: Hou et al., Long-term ultrasound-enhanced convective injection device for neural drug delivery, Device (2026), https://doi.org/10.1016/j.device.2026.101333

49% HF and DI water—of the SiO_2 underneath the piezoelectric/electrodes stack. The undercut pattern is held together by the anchor layer and then picked up using thermal release tape (Revalpha 90°C), thus maintaining the element-to-element orientation before being transferred to a second Si wafer.

A release layer (Kayaku OmniCoat) was spin coated on the second Si donor wafer and cured above 130°C. After this, a 1.1-μm layer of SU-8 TF 6001 was spin coated, underexposed (3.5 s with 365-nm UV light), and soft baked; this layer served as the encapsulation of the device and a sticky substrate for the transfer of the thin-film stack. The thermal release tape with the thin-film stack was pressed onto the SU-8 layer, and the wafer was brought to a temperature above the release threshold (>90°C) for 5 min, after which the tape was carefully removed. Acetone, isopropanol (IPA), and DI water were sprayed on the wafer for removal of any anchor layer or thermal tape residues.

To promote adhesion between SU-8 layers, O_2 plasma treatment (RIE) is applied. A 0.8-μm SU-8 2000.5 layer is spin coated, exposed, developed, and cured (hard baked). The layer covered the device outline everywhere but in the electrodes' openings, in preparation for the physical deposition of metals to form electrical traces. 10 nm of Cr and 200 nm of Au were sputter deposited (AJA ATC Orion 5), then patterned with 1.6-μm positive PR (Microchem AZ5214-W), and subsequently etched with gold and CR-7 etchant (Transene). The subsequent steps are related to the creation of the flexural membrane and the cavity walls of the pMUT. After another round of O_2 plasma exposure, a 0.8-μm flexural membrane layer was spin coated with SU-8 2000.5, exposed with 365 nm UV, developed, and hard baked (slowly heated to 120°C, kept at temperature for 5 min). The tall cavity walls (40 μm) were constructed by O_2 plasma exposure, followed by spin-coating the more viscous SU-8 2050, which was then patterned, developed, and hard baked.

To finalize the pMUT structure constructed in the top-down approach, a backing layer is needed to seal the air cavities, preferably minimizing SU-8 infiltration in the cavity. For that end, a polyethylene terephthalate (PET) film is spin coated with a sacrificial layer of polyvinyl alcohol (PVA) (4 wt %), and annealed for 2 min at 120°C. Then, a 10-μm layer of SU-8 3010 is spun on the PET film and soft baked. The Si donor wafer containing all the thin-film and SU-8 structures undergoes RIE O_2 plasma treatment and is heated to 95°C. The PET film is gently dropped on top of the wafer, allowing the SU-8 layers to touch. After observation under the microscope (10× objective), confirming that the SU-8 layers have come in contact, the wafer + PET film union underwent UV exposure and development, after which the PET film was removed gently. Finally, the pMUT array device was completely encapsulated, but still connected to the Si wafer substrate. After two-photon lithography for microfluidic cannula fabrication on the mounted wafer, the devices undergo final release through a dry etch (RIE, CF4/O2) RIE protocol for 1–1:30 min (to expose the release layer of Omnicoat) and subsequent immersion in MF-26A developer (Kayaku Advanced Materials), which dissolves the sacrificial Omnicoat layer and makes the LUCID devices detachable from the Si wafer. After IPA, water rinse, and N_2 drying, the posterior face of the device (the bond pad size) undergoes dry etch (RIE, $CF4/O_2$) with a shadow mask to make the pads accessible to ACF connections. Assembly is completed under a microscope with polyimide tapes, where bond pads are connected to the ACF and that to a PCB.

Two-photon lithography for microfluidic cannula fabrication

The microfluidic injection cannula was produced using a two-photon lithography system (NanoOne, UpNano GmbH, Austria), which allows for 3D printing with minimal horizontal and vertical features of 170 and 550 nm, respectively. The devices were printed with a 10× objective (Olympus) in vat mode with 5 μm layer height, using the biologically compatible UpPhoto resin as a substrate. Four fiducial markers with known coordinates were lithographically defined on the wafer substrate with the microfabricated pMUT structure, which was built in an inverted manner such that the bottom side of the pMUT array is exposed to resin as a substrate for printing. The print is aligned to the translation and rotation of the fiducial markers relative to the printer's coordinate system, so the print is computationally aligned to pMUT devices on wafer. Following the completion of the print, the devices are soaked in isopropyl alcohol for 1 h until unexposed resin has been properly flushed out of the microfluidic channels. To release the completed devices from the wafer with *in situ* prints, the initial Omnicoat (Kayaku) layer is dissolved in dilute NaOH developer (MICROPOSIT MF CD-26).

Wireless drive electronics

Architecturally, the implantable PCB design centers around a wireless charger, Bluetooth module, and charge pump for driving the pMUT. For this board, all pMUT elements are driven in parallel. Wireless communication is provided via a Bluetooth module (ISP1807). Power is delivered wirelessly using inductive coupling and managed by the LTC4124 wireless power receiver. A LiPo cell rated at 3.7 V/110 mAh provides energy storage, with an LDO regulating the supply down to 3.3 V for digital and control circuitry.

To generate the higher voltages required to drive the PMUTs, a dedicated piezo driver (PAM8904) is used. This device functions as a charge pump, boosting the available supply voltage to approximately 10 V, enabling sufficient diaphragm excitation while remaining within implant-safe voltage limits.

Wireless power transfer works by the same principle as a transformer: an alternating current through a transmitter (TX) coil produces an oscillating magnetic field, which induces a voltage in the implanted receiver (RX) coil. Unlike a transformer, however, there is no shared magnetic core to guide flux from one coil to the other (wireless chargers are sometimes termed "air-core transformers"). Without a shared magnetic core, the vast majority of magnetic flux never reaches the RX coil. This "loose coupling" is the central challenge of inductive power transfer. To combat the inefficient power transfer, we use resonant inductive charging. By adding a capacitor to each coil to form an LC tank and tuning both to the same frequency, energy builds up over many cycles, and transfer efficiency is maximized.

We center our design on the LTC6990 and LTC4124 (Analog Devices). The LTC4124 is an integrated wireless power receiver that combines rectification of the induced AC voltage with battery charging management, implementing a

Please cite this article in press as: Hou et al., Long-term ultrasound-enhanced convective injection device for neural drug delivery, Device (2026), https://doi.org/10.1016/j.device.2026.101333

constant-current/constant-voltage profile suitable for LiPo cells. The LTC6990 is a programmable oscillator that drives the TX coil through a switching field-effect transistor (FET), with its output frequency set by a single resistor.

Driving frequency bounds

The selection of the coils and capacitors in the LC tanks accommodates the constraint of TX frequency. Since FETs are used to produce the alternating current in the TX coil described above, their input capacitance (and the LTC6990 output driver resistance) sets the gate RC time constant:

$$\tau = R_{drive} \cdot C_{iss} = 150\Omega \times 126\,pF = 18.9\,ns.$$

To ensure that the FET switches cleanly within each cycle, we require τ to occupy no more than 20% of the waveform period T. This yields a minimum period of

$$T_{min} = \frac{\tau}{0.20} = 94.5\,ns \Rightarrow f_{max} = 10.6\,MHz.$$

All subsequent frequency choices are bound by this constraint.

Receiver coil selection

The receiver (RX) coil was selected from the coils recommended in the LTC4124 datasheet to meet the footprint and inductance requirements: Würth 760308101208, with an inductance of 13 μH.

Receiver coil capacitor selection and operating frequency

The RX capacitance for the maximum allowable frequency (10.6 MHz) is

$$C_{min} = \frac{1}{(2\pi f_{max})^2 L_{RX}} = 17\,pF.$$

We select C_{RX} = 1.0 nF, a standard value comfortably above this floor, yielding an RX resonant frequency of

$$f_{RX} = \frac{1}{2\pi\sqrt{13\,\mu H \times 1\,nF}} = 1.40\,MHz.$$

TX LC tank design

Typically, TX and RX resonant tanks in wireless chargers are tuned to the same resonant frequency. However, the LTC4124 datasheet specifies that driving the TX LC tank at approximately 1.29× the RX resonant frequency enables zero-voltage switching (ZVS) in the half-bridge driver. Under ZVS, the FET switches when the drain voltage is near zero, eliminating capacitive discharge losses and substantially reducing switching-related heat dissipation. The target TX resonant frequency is therefore:

$$f_{TX} = 1.29 \times f_{RX} = 1.80\,MHz.$$

We select the Würth 760308103206 coil (L_{TX} = 7.5 μH) with C_{TX} = 1.0 nF, giving f_{TX} = 1.84 MHz. We confirm that the peak TX coil current is under 1.5 A, and the maximum current rating is

$$I_{TX-PEAK} = \frac{0.36 \cdot V_{IN}}{f_{TX-TANK} \cdot L_{TX}} = 133\,mA < 1500\,mA.$$

Impedance spectroscopy characterization

Impedance spectra of assembled LUCID devices in DI water were acquired using an Agilent E4990A impedance analyzer over 50 kHz–1 MHz. The measurement fixture introduced a parallel cable capacitance that dominated the raw response. To isolate the piezoelectric contribution, the cable capacitance was estimated from the high-frequency tail of the measured admittance (Y = 1/Z), where the device impedance is large and the response is governed primarily by Y_cable = jωC_cable. The median of Im(Y)/ω over the upper 10% of the frequency range yielded C_cable ≈193.5 pF for the representative device DEV-A10. The cable admittance was subtracted point by point, Y_corrected = Y_measured − jωC_cable, and corrected impedance computed as Z_corrected = 1/Y_corrected. Resonance (f_r) and anti-resonance (f_a) frequencies were identified as the frequencies of minimum and maximum |Z_corrected|, respectively (f_r = 352.8 kHz, f_a = 487.0 kHz for DEV-A10).

Scanning laser Doppler vibrometer measurements

Resonance responses of assembled LUCID devices in DI water were acquired using an MSA-500 Laser Doppler Vibrometer (Polytec GmbH, Germany) over 50 kHz–1 MHz. A built-in signal generator enables custom excitation ranging from chirped sine waves to pure sine and square waves, which are synchronized to interferometric Doppler measurements and produce frequency spectra and displacement characterizations corresponding to the device actuation. Out-of-plane displacement was captured in an array corresponding to the surface of each of the elements of the pMUT array. To capture resonant behavior and performance in a physiological medium, water is used to simulate the mechanical coupling, and LDV measurements are taken of the device while submerged.

Hydrophone pressure measurement

Measurements were acquired in DI water using a calibrated fiber-optic hydrophone (Precision Acoustics FOHS v.2; nominal sensing diameter 100 μm) on a fixed gantry. A manual four-axis micromanipulator (TOAUTO) with 25-μm graduations controlled relative positioning over a nominal 25- to 250-μm scan. Reported distances are nominal micromanipulator positions. Devices were driven at 300 kHz using five pulses with a 100-ms pulse period and varying drive voltages. Hydrophone output was recorded with a PicoScope 5444D MSO, which automatically averaged peak-to-peak voltage measurements over the last 16 acquisitions. Peak-to-peak pressure was calculated as $p_{pp} = V_{pp}/S$ using the calibrated sensitivity S at the drive frequency. Peak rarefactional pressure, the magnitude of the negative pressure excursion, was estimated as $p_r \approx p_{pp}/2$ for the MI calculation under an approximately symmetric sinusoidal-waveform assumption. No tissue derating was applied.

Please cite this article in press as: Hou et al., Long-term ultrasound-enhanced convective injection device for neural drug delivery, Device (2026), https://doi.org/10.1016/j.device.2026.101333

COMSOL simulation of acoustic streaming

Finite-element simulations of pMUT actuation, acoustic radiation, and acoustic streaming were performed in COMSOL Multiphysics 6.1 (build 282; Acoustics Module + Particle Tracing Module) on a representative three-element subset of the 24-element pMUT array. The model was built in 2D to keep the streaming and particle-tracing physics tractable while preserving the dominant cavity-mode behavior; each pMUT in the model used a stack and dimensions matching the fabricated device: a 1-μm piezoelectric layer between a 250-nm Pt bottom electrode and a 250-nm Au top electrode, a 1-μm SU-8 flexural membrane, an air-filled cavity of 140 μm diameter and 25 μm depth bounded by 20-μm SU-8 walls, a 25-μm SU-8 backing layer, and a 500-nm SU-8 encapsulation. The fluid domain above the array was filled with water (COMSOL "Water, liquid" library material) and terminated by a perfectly matched boundary to model unbounded radiation; the two-photon-printed cannula resin was approximated with Poly(methyl methacrylate) (PMMA) library properties (temperature-dependent E(T), ν(T), and ρ(T)).

Material properties used in the structural and electrical domains were SU-8 (ρ = 1190 kg/m^3, E = 4.02 GPa, ν = 0.22), gold (ρ = 19,300 kg/m^3, E = 70 GPa, ν = 0.44), and platinum (ρ = 21,450 kg/m^3). For the piezoelectric layer, the model used the built-in lead zirconate titanate (PZT-5H) library material (ρ = 7,500 kg/m^3; full anisotropic elasticity matrix; coupling coefficients $e_{31} = -6.62$ C/m^2, $e_{33} = 23.24$ C/m^2, $e_{15} = 17.04$ C/m^2; relative permittivity ε_r = {1,704, 1,704, 1,434}) as an engineering approximation for the experimentally used KNN piezoceramic. Because the flexural-mode resonance of a thin-membrane pMUT is set predominantly by membrane geometry and stack stiffness rather than by the specific piezoceramic, this substitution affects absolute drive efficiency more than mode shape or resonant frequency; the experimentally measured displacement vs. voltage relationship (Figure 2F) was used to anchor the model's absolute pressure output.

Five physics interfaces were coupled in the model: (1) solid mechanics and (2) electrostatics, coupled by a piezoelectric effect multiphysics node (stress-charge constitutive form) to capture the actuation of the array; (3) pressure acoustics, frequency domain (including thermoviscous boundary layer impedance and shell boundary subnodes) to capture viscous and thermal dissipation at the solid-fluid interfaces that govern streaming; (4) laminar flow, with an acoustic streaming multiphysics coupling that drives the slow mean-flow field from the time-averaged Reynolds stresses of the first-order acoustic field; and (5) particle tracing for fluid flow, used to compute trajectories of 3-μm tracer particles released into the streaming field for direct comparison with the experimental PTV data (Figures 3D, 3F, and 3G). Drive was applied through a terminal voltage on the top electrode and a ground on the bottom electrode in the electrostatics interface.

Two studies were performed: an eigenfrequency study to identify the fluid-loaded flexural-mode resonance of the cavity and a frequency-domain study around a "frequency of interest" parameter fr_i (set in the model to 450 kHz, with sweeps around the eigenfrequency to span a comprehensive frequency range) used to compute the steady-state acoustic pressure field, the streaming flow field, and the particle trajectories. All fields were discretized with quadratic Lagrange elements; the mesh combined a swept boundary-layer mesh adjacent to solid-fluid interfaces (to resolve the thermal and viscous boundary layers required by the thermoviscous formulation), free-triangular elements in the bulk water domain (sized for adequate elements per acoustic wavelength using COMSOL's wavelength-based sizing), and refined elements at the cavity corners. The typical wave speed for the PML was set to the speed of sound in water. Output fields (acoustic pressure, particle velocity, time-averaged streaming velocity, and particle trajectories) were exported as VTU and CSV files and overlaid on the PTV measurements using custom Python scripts.

Particle tracking velocimetry

Acoustic streaming at the LUCID cannula outlet (Figures 3D–3F) was visualized using fluorescent particle tracking, performed on the optical column of the LDV bench used for the acoustic characterization measurements. Red-fluorescent polystyrene microspheres (3.1 μm nominal diameter, 2.5% solids; Magsphere Inc., catalog/Lot PSFR5370) were suspended in DI water above an operating LUCID device. The device was oriented in profile (side view) under the LDV so that the pMUT array surface, the cannula outlet, and the water column above the array were all visible in a single imaging plane; the suspension was illuminated with a green excitation laser to drive the particle fluorescence and maximize bead-to-background contrast against the dark water background. Imaging used an infinity-corrected Mitutoyo 5× long-working-distance objective with the LDV bench's built-in camera capturing 30-fps video. Through-plane motion was sampled by stepping the objective focus to bring imaging planes at different depths into focus, both above and below the pMUT array profile. The device was driven at its resonance frequency (~300 kHz) and 10 V_{pp} throughout the recording, matching the bench acoustic-characterization protocol.

Particle trajectories were extracted from each video using a custom Python pipeline built on TrackPy (Crocker-Grier feature localization and linking). Each frame was converted to grayscale, contrast enhanced (multiplicative gain 1.03), sharpened with an unsharp mask (strength 1.93; σ_blur = 1 px), and intensity inverted before band-pass feature localization (tp.locate; particle diameter ≈7 px, minimum integrated brightness 100, minimum inter-feature separation 5 px). Detected features were linked into trajectories (tp.link_df; maximum frame-to-frame displacement 9 px, memory of 3 frames to bridge short occlusions), trajectories shorter than 10 frames were rejected (tp.filter_stubs), and per-particle instantaneous velocities were smoothed with a 5-frame rolling average. Pixel-to-physical scaling was established by an in-frame two-point calibration in the GUI against a known device feature (e.g., the cannula outlet diameter) in the same focal plane.

Time-averaged streaming velocity fields and streamlines (Figures 3B, 3D, and 3F) were obtained by binning the per-particle velocity vectors onto a regular spatial grid, averaging within each grid cell over the scan duration, and interpolating to fill cells with no direct samples. Streamlines were integrated through the interpolated field using Matplotlib's streamplot routine. Line

Please cite this article in press as: Hou et al., Long-term ultrasound-enhanced convective injection device for neural drug delivery, Device (2026), https://doi.org/10.1016/j.device.2026.101333

profiles along the cannula axis (Figures 3E and 3F) were extracted from the same interpolated field and overlaid on the corresponding COMSOL streaming simulation for the direct experiment vs. simulation comparison shown in Figure 3.

PCB power characterization

Power consumption and wireless-charging behavior of the LUCID custom PCB were characterized in a benchtop setup using a Joulescope JS220 precision DC measurement instrument (Jetperch LLC; instrument serial JS220-005756) placed in-line at the battery terminal so that all current flowing into or out of the on-board Li-ion cell was captured. The PCB was operated under its production firmware (NRF52840 SIP, BLE service active, integrated boost converter + piezo driver) and the US stage, when enabled, drove a connected LUCID device at the device resonance with 10 V_{pp} at 50% duty cycle (pulse repetition frequency 1 kHz). Wireless charging was supplied through the on-board resonant inductive coil paired with the bench charging transmitter.

A single continuous I-V-P trace (battery current i(t), battery voltage v(t), and instantaneous power p(t) = v · i) was logged through four operating regimes that were commanded sequentially over the paired mobile-app interface: (1) wireless charging only, (2) idle while BLE-connected (no US, no charging), (3) US-ON with charging disabled, and (4) US-ON during simultaneous wireless charging. Each regime was held for ≥30 s after entry so that any mode-switching transient occupied only a small fraction of the analysis window.

The Joulescope battery-terminal probe sign convention was retained throughout: positive current denotes net discharge (power delivered from the battery to the PCB), and negative current denotes net energy flowing into the battery from the charging coil.

Agarose phantom preparation

Realistic brain tissue phantoms were created, with 0.6% agarose gel, as described in Chen et al.[50] Agarose powder was mixed with 1× TBE and DI water, stirred and heated until boiling, and then cooled for 5 min before being poured into 30-mm-diameter petri dishes.

Rhodamine B dye preparation

Rhodamine B powder (Sigma-Aldrich, R6626, molecular weight 479.01 Da) was dissolved in 1× TBE buffer to prepare a 1 mM stock solution. The dye (powder) was added gradually to the buffer and mixed vigorously using a magnetic stirrer until fully dissolved, yielding a homogenous solution. This concentration was selected as appropriate for phantom testing because the assay was performed under bright-field imaging rather than fluorescence microscopy. The solution was stored protected from light until use.

Acute *in vitro* dye infusion

Tissue-mimicking phantom gels and the rhodamine B infusate were prepared as described above. For each acute experiment, 5 μL of the infusate was delivered through the LUCID cannula by a Hamilton gas-tight syringe driven on an NE-300 InfusionONE programmable syringe pump (New Era Pump Systems) at 0.5 μL/min for 10 min; the syringe pump was then halted and the phantom imaged for a further 10 min, yielding a total acquisition window of 20 min per run.

In the US-ON condition, the LUCID array was driven continuously across the full 20-min window by a benchtop function generator (Agilent HP 33120A), producing a sinusoidal output at the device's resonance frequency (which fell between 300 and 400 kHz across devices) with 10 V_{pp} amplitude, a 25% duty cycle, and a 1 kHz pulse-repetition frequency (PRF). In the matched US-OFF condition, the same device was operated with the function-generator output disabled while all other parameters (infusate volume, infusion rate, phantom batch, and optical setup) were held constant. Bright-field time-lapse images of the dye-distribution front were captured at 1-min intervals over the 20-min window with an Olympus SC50 CMOS camera coupled to a Navitar Zoom 7000-2 fixed-magnification lens (Navitar/Amentek), under matched illumination and exposure between the US-ON and US-OFF runs. Image stacks were quantified through the segmentation and area-calculation pipeline in dye_diffusion/analyze_diffusion.py to extract dye area as a function of time.

The acute assay used a paired, within-device design to limit variation due to cannula-tip geometry, gel homogeneity, and mounting. Each of the four devices contributed one US-ON run and one independently acquired US-OFF control run. The order of runs was randomized, and devices were dried and primed before insertion into a pristine region of gel. Within-device differences (US-ON minus US-OFF, normalized to the corresponding US-OFF trace) were calculated at each 1-min sample point. Figure 4E shows normalized dye-area trajectories. Figure 4F compares within-device dye-area growth rates during pump activation (0–10 min) and after pump cessation (10–20 min), using paired two-sided *t* tests.

Chronic *in vitro* dye infusion

Tissue-mimicking phantom gels were prepared with 0.6% (w/v) agarose dissolved in 1× TBE buffer; the mixture was heated until boiling, cooled briefly, and poured into the imaging container. The fluorescent payload was prepared by dissolving tetramethylrhodamine isothiocyanate (TRITC)-dextran (average molecular weight 65,000–85,000 Da; Sigma-Aldrich, catalog T1162) in 1× TBE at a final concentration of 1 μM.

Continuous infusion was driven by an Alzet osmotic pump (model 1003D; 100 μL reservoir capacity; nominal delivery rate 1 μL/h) filled with the TRITC-dextran infusate and connected to the barbed inlet of the LUCID device through a length of silicone tubing. Because the Alzet 1003D pump reaches its nominal delivery rate only at body temperature, each pump was submerged in a temperature-controlled water bath held at 37.0°C using a flexible resistive heating strip (Meccanixity) driven through a MOSFET by a PID control loop (Teensy 4.1) with thermocouple feedback. Feedthroughs were drilled into the base of the bath enclosure to allow the silicone tubing to pass out to the LUCID inlets and were sealed with epoxy to prevent leakage; the LUCID device head and the phantom gel were positioned outside the bath at ambient temperature so that imaging was unobstructed and unaffected by bath optics. Both pumps were primed for 2 h in the heated bath prior to the start of the

Please cite this article in press as: Hou et al., Long-term ultrasound-enhanced convective injection device for neural drug delivery, Device (2026), https://doi.org/10.1016/j.device.2026.101333

experiment to clear trapped air from the tubing and to confirm steady, equal flow at both pump outlets before connecting to the LUCID devices.

For each experimental session, two devices were imaged in parallel: one device was connected to the wireless PCB controller (US-ON arm) and the other was operated with the wireless drive disabled (US-OFF control), while both devices shared the same heated bath, infusate batch, and phantom slab, in order to minimize between-arm confounds. The US-ON device was driven for the full 20 h under a 20-min ON/20-min OFF cycle. Within each ON window, the array was driven at the device resonance frequency (~300 kHz) with a 10 V_{pp} sinusoidal drive and a 25% pulse-repetition duty cycle (PRF = 1 kHz). The 25% duty cycle was chosen to remain within the chronic $\leq 2^{\circ}$C thermal-rise envelope established by the duty-cycle sweep in Figure 4B ($\Delta T = 1.53 \pm 1.01^{\circ}$C at 25% DC under submerged-water bench conditions); the 20-min/20-min cycle further limits the time-averaged on-time to 50% of the experiment. Time-lapse images of the dye-distribution front in each phantom were acquired under matched illumination and exposure between the US-ON and US-OFF arms and quantified through the segmentation and area-calculation pipeline described in the "acute *in vitro* dye infusion" subsection above.

To suppress evaporative drift over the 20-h acquisition window, the phantom imaging dish and heated bath were covered with a transparent lid throughout the experiment, and ambient temperature and relative humidity in the imaging enclosure were logged continuously alongside the bath temperature to confirm that the dish was at a stable external environment for the duration of the run. Time-lapse video of the dye-distribution front in each phantom was recorded with an iPad Pro (M4; Apple, Inc.) in its native time-lapse mode, with the device fixed on a stationary mount above the phantom and the two arms in a single frame to ensure matched illumination in a brightly-lit photobox, optical path, and exposure between the US-ON and US-OFF channels. The resulting time-lapse video was decoded into a sequence of frames at the iPad's automatic capture cadence over the 20-h window and quantified through the segmentation and area-calculation pipeline described in the "acute *in vitro* dye infusion" subsection above.

Animal welfare

Animal procedures were performed in accordance with the Brigham and Women's Hospital Institutional Animal Care and Use Committee (IACUC protocol 2024N000132; PI: M. Mineo), the Boston University Institutional Animal Care and Use Committee (IACUC protocol 201800579; PI: Steve Ramirez), and the NIH Guide for the Care and Use of Laboratory Animals.

In vivo MRI Gd contrast experiment

Adult male C57BL/6 mice (8 weeks of age; The Jackson Laboratory) were anesthetized with isoflurane (3% induction, 1.5% maintenance) and received pre-operative meloxicam (5 mg/kg, subcutaneous [s.c.]) and buprenorphine SR-Polymer (1 mg/kg, s.c.) for analgesia. Mice were positioned in a Kopf Model 900LS stereotaxic frame; the scalp was shaved, disinfected, and infiltrated with lidocaine (2 mg/kg). A 0.6 × 1.5-mm slit incision was made, and a burr hole was drilled through the skull using a 0.6-mm round-burr Micro-Drill bit (Roboz MD-6280C-½) at AP +0.5 mm and ML +1.5 mm relative to bregma. The infusion device (LUCID microfluidic cannula or, for the syringe arm, a 26-gauge 30°-beveled Hamilton 1700-Series Gastight syringe) was lowered to DV −3.0 mm at 3 mm/min, with no pre-infusion dwell. Each animal received 2 μL of gadobutrol (Gadavist, Bayer, 604.7 Da; donated by Mass General Brigham Radiology) diluted 1:100 in medical-grade saline, infused at 0.2 μL/min over 10 min. The device was then held at depth for an additional 10-min post-infusion dwell, withdrawn at 3 mm/min, and the craniotomy closed with 5-0 nylon suture.

For LUCID arms, US was applied during the 10-min post-infusion dwell only (i.e., after the 2-μL infusion completed) at 10 V_{pp} drive and a 30% duty cycle, at the device resonance frequency (which fell between 300 and 400 kHz across devices). Gadobutrol is a hydrophilic, low-molecular-weight gadolinium chelate that does not cross the intact BBB; the contrast distribution observed in our experiments, therefore, reflects direct intracortical delivery and subsequent interstitial transport, not vascular uptake. This is a deliberate design choice: by using a contrast agent excluded by the intact BBB, the comparison between syringe CED and LUCID UECD isolates the mechanical/convective enhancement provided by acoustic streaming from any potential BBB-disrupting effect of the US.

Approximately 1 h after the end of infusion, mice were transferred under continuous isoflurane anesthesia to a 3 T Bruker BioSpec scanner equipped with a small-animal cryocoil. T1-weighted images were acquired with a Bruker:RARE sequence: TR = 1,000 ms; effective TE = 10 ms; RARE factor = 2; flip angle 90° (excitation)/180° (refocus); 3 averages; matrix 192 × 192; field of view 20 × 17.17 mm; in-plane resolution 0.104 × 0.089 mm; slice thickness 1 mm; 15 contiguous axial slices, no slice gap; receive bandwidth ≈26 kHz; total scan time 4 min 48 s. A pre-contrast T1 baseline was not acquired for the experimental session; sessions in which the injection failed (no visible contrast at the target) were excluded from analysis prior to segmentation.

Contrast-enhanced volumes were quantified from three contiguous coronal slices per animal centered on the injection site, using a custom Python segmentation pipeline. A region-growing intensity threshold (89.5%–97.5% of the per-slice maximum signal, optimized per slice) was applied around the injection seed point to delineate the gadolinium-enhanced region while excluding ventricular and skull-edge signal. Per-animal volume was computed as the sum of the three slice areas multiplied by the 1-mm slice thickness. Group comparisons ($n = 5$ per arm) used an unpaired two-sided Student's t test (scipy.stats.ttest_ind), with $\alpha = 0.05$.

Péclet-number analysis across different flow conditions

For each delivery regime we computed Péclet numbers to compare advective and diffusive transport on a common axis. The bolus equivalent radius was taken as $r = \sqrt{A/\pi}$ from the segmented dye area A (*in vitro* experiments) or as the spherical-equivalent radius $r = \sqrt[3]{\frac{3V}{4\pi}}$ from the segmented contrast volume V (*in vivo* MRI). The pump-only Péclet number was defined in the radial convection-enhanced-delivery convention as

Please cite this article in press as: Hou et al., Long-term ultrasound-enhanced convective injection device for neural drug delivery, Device (2026), https://doi.org/10.1016/j.device.2026.101333

$Pe_{pump} = \frac{Q}{4\pi rD}$, evaluated at the mean measured bolus radius, where Q is the nominal volumetric pump rate. The observed Péclet number was defined as $Pe_{obs} = \langle r \rangle \cdot \frac{dr/dt}{D}$, with dr/dt obtained by ordinary-least-squares regression of r against time over the interval of interest and ⟨r⟩ the mean radius over that interval; for the single-time point *in vivo* MRI data, the equivalent form $Pe_{obs} = \frac{r^2}{2 \cdot D \cdot t_{total}}$ was used, with t_total = 1 h from injection to imaging. The *in vivo* Péclet comparison is, therefore, derived from the MRI volume comparison and is not an independent measurement of bolus-front velocity. Because Pe ∝ 1/D, absolute Pe values scale with the assumed diffusivity, but the LUCID-on/-off ratio within a given tracer is independent of D. Diffusivities were literature-based approximations for the Péclet analysis. For Rhodamine B in 0.6% agarose, we used the aqueous-solution value $D = 4.2 \times 10^{-10}$ m^2 s^{-1},[65] assuming negligible additional gel hindrance. For TRITC-dextran (65–85 kDa), we used a nominal $D = 4.0 \times 10^{-11}$ m^2 s^{-1}, based on approximately 3.8×10^{-11} m^2 s^{-1} for fluorescent 70-kDa dextran in 0.3% agarose at 34°C[66]; applying this value to our 0.6% agarose phantom is an approximation. For gadobutrol (Gadavist), $D = 1.5 \times 10^{-10}$ m^2 s^{-1} was estimated for brain extracellular space using $D = D_{free}/\lambda^2$,[2] with the Gd-DTPA free-solution value $D_{free} = 3.8 \times 10^{-10}$ m^2 s^{-1} and tortuosity λ = 1.6 as a literature-based proxy.[67] These diffusivities were not measured directly in our phantoms or tissue. Group comparisons of Pe_{obs} used Welch's unequal-variance *t* test. For purely 2D radial diffusion ($r^2 \propto 4Dt$), Pe_{obs} asymptotes to ≈2, which we use as a passive-diffusion reference (Figure S15).

Within-bolus uniformity was quantified only for the chronic *in vitro* TRITC-dextran phantom experiment, using the segmented dye region, as the coefficient of variation (CV = σ/μ) of intensity across all bolus pixels and as the center-to-edge intensity ratio (mean intensity within the inner half of the bolus radius divided by the mean within the outer half). Pixels corresponding to the infusion cannula were identified from the change in lab lightness relative to the dye-color signal and excluded from these metrics.

Tumor-bearing model, contrast experiment

CT-2A glioma cells stably expressing firefly luciferase (CT-2A/fLuc) were stereotaxically inoculated into the right striatum of adult male C57BL/6 mice (8 weeks; The Jackson Laboratory) under the same anesthesia and analgesia regimen described for the naive cohort. 5×10^4 cells suspended in 3 μL of sterile PBS were injected at AP +0.5 mm, ML +1.5 mm, DV −3.0 mm from bregma. Seven days after inoculation, tumor-bearing animals underwent the same LUCID cannula implantation and Gadavist infusion protocol described above, with US on (n = 1) or off (n = 1). MRI imaging followed the same protocol, and 1-h delay was used for the naive cohort. Given the single-subject group size, the tumor-bearing cohort is reported here as illustrative only; no statistical comparison is performed.

Tumor-bearing model: CD3/CD8 recruitment experiment

GBM tumors were established in 7- to 8-week-old C57BL/6J mice by stereotactic injection of 50,000 SB28-GFP cells in 2 μL into the left prelimbic cortex (coordinates relative to bregma: AP +1.8 mm, ML +0.5 mm, DV −2.5 mm), with anesthesia induced at 3% isoflurane and maintained at 1.5%–2% throughout surgery. Tumors were allowed to grow for 13 days, with animals pair-housed, after which the US devices were implanted on day 14 at the same AP/ML coordinates to a depth of 3.0 mm. In the US-ON group, the LUCID transducer was driven near its resonant frequency (∼300 kHz) at a peak-to-peak drive of 10 V_{pp} with a 50% duty cycle, for a total treatment duration of 20 min, using a benchtop function generator (Agilent HP 33120A) via a percutaneous connection; the implantable wireless PCB was not used in this experiment. US-OFF control animals received an identical device implantation and an identical anesthesia and handling protocol but no acoustic stimulation. The 50% duty cycle used in this bounded 20-min session consumes approximately 10% of the 202-min exposure budget derived for 50% duty cycle at the 2-CEM43 threshold (Note S2) and is therefore within the thermal envelope. The ≤25% duty-cycle recommendation given in the "discussion" section applies to sustained chronic operation, in which cumulative thermal dose accrues without a defined endpoint. Devices in both groups were explanted at the end of the 20-min session on day 14; no device remained *in situ* beyond that session. Animals were then monitored without implants through days 15–17 and euthanized on day 18 by isoflurane overdose and transcardially perfused with cold PBS followed by 4% paraformaldehyde (PFA); brains were then post-fixed in 4% PFA for 48 h.

Fixed brains were sectioned at 40 μm on a vibratome, and CD3/CD8 immunohistochemistry was performed on 2–3 sections per animal. T cells were labeled with an anti-CD3 antibody (Thermo Fisher, clone 17A2, Cat# 14–0032-82; 1:400) and an anti-CD8α antibody (Abcam, clone EPR21769, ab217344; 1:500), detected, respectively, with Alexa Fluor 488 goat anti-rat IgG (H + L) (Thermo Fisher, A-21434) and Alexa Fluor 594 goat anti-rabbit IgG (H + L) (Thermo Fisher, A-21245), both at 1:200. Confocal z stacks (2 μm spacing) were acquired for each region of interest (ROI) and segmented in Cellpose; CD8 quantification was subsequently refined in CellProfiler, restricting counts to $CD8^+$ objects colocalizing with $CD3^+$ signal to ensure specificity for T cell populations. To minimize edge artifacts and brightness variability, only central Z-planes (Z = 5 to Z = max − 2) were analyzed, and counts were averaged across adjacent planes to account for the typical T cell diameter (∼5–10 μm) and reduce double-counting. Per-stack means were averaged across ROIs within each anatomical zone and then across sections, yielding a single standardized per-region value for each animal.

Animal welfare and euthanasia

Mice were group-housed under a 12 h/12 h light-dark cycle with *ad libitum* access to standard chow and water. Following all imaging procedures, animals were euthanized by 5% isoflurane overdose followed by transcardial perfusion with 0.9% sodium chloride.

Statistics and reproducibility

Statistical analyses were performed in Python with NumPy, SciPy, and pandas (scipy.stats); MATLAB (vR2024b; MathWorks, Statistics and Machine Learning Toolbox) was used for the implantation test, thermal trace processing (Figures 4A and 4B), and CD3/CD8

Please cite this article in press as: Hou et al., Long-term ultrasound-enhanced convective injection device for neural drug delivery, Device (2026), https://doi.org/10.1016/j.device.2026.101333

immunohistochemistry analysis. Acute dye-growth comparisons (Figure 4F) used paired two-sided *t* tests across matched device runs. Implantation-force and MRI contrast-volume comparisons used unpaired two-sided Student's *t* tests; the MRI cohort comprised $n = 5$ animals per arm. Observed Péclet comparisons used Welch's unequal-variance *t* test, with mean ± SEM and replicate counts reported in Table S3. Other continuous summaries are mean ± SD across the replicates specified in the figure legends. Significance was set at $\alpha = 0.05$. Linear fits to the 20-h dye-area curves (Figure 5D; $n = 1$ device pair) used ordinary least-squares regression, with 95% confidence intervals on the slope and R^2 reported. PCB power means and SDs were computed over the trailing 60% of each labeled operating phase (Figures 5E–5G). No multiple-comparison adjustment was applied outside the CD3/CD8 analysis described below.

The CD3/CD8 immunohistochemistry analysis (Figure S17) used a different statistical framework tailored to its repeated-measures design: a linear mixed-effects ANOVA (count $\sim$ condition $\times$ region, with animal as a random intercept), fit separately for $CD3^+$ counts, $CD8^+$ counts, and the $CD8^+$:($CD3^+CD8^-$) ratio, with fixed effects assessed by F tests using residual denominator degrees of freedom. Planned per-region contrasts (Welch's two-sided *t* test) were corrected for multiple comparisons across the three regions using the Bonferroni method. Where Lilliefors testing indicated non-normality, Welch's *t* test results were corroborated with Mann-Whitney U tests.

RESOURCE AVAILABILITY

Lead contact

Requests for further information and resources should be directed to and will be fulfilled by the lead contact, Canan Dagdeviren (canand@media.mit.edu).

Materials availability

This study did not generate new, unique reagents. CAD files are available. Other design files may be available upon request.

Data and code availability

All data of this study are available upon reasonable request from the lead contact. The LUCID_BLE firmware is available at GitHub: jasonf-hou/LUCID_BLE and the and LucidBLE iOS app source is available at GitHub: jasonf-hou/LucidBLE.. Raw data can be found at Figshare: https://doi.org/10.6084/m9.figshare.32817401 and at OpenNeuro: ds008214 (*in vivo* data).

ACKNOWLEDGMENTS

This work was supported by the MIT Media Lab Consortium and by NIH R01 NS134723 and P01 CA163205 (to E.A.C. and M.M.), the MIT HEALS Fellowship (J.F.H), and the MIT Presidential Fellowship (S.B.O.). The authors thank the staff of MIT.nano and the YellowBox cleanroom of the Conformable Decoders Group at the MIT Media Lab for fabrication support, Alan Han and the Center for Bits and Atoms for the use of the Instron tool, the Brigham and Women's Hospital animal facility and Department of Neurosurgery for surgical and imaging support, and Mass General Brigham Radiology for the donation of Gadavist (Bayer) contrast agent.

AUTHOR CONTRIBUTIONS

Conceptualization, J.F.H., S.B.O., M.O.N., H.L., M.M., S.R., and C.D.; methodology, J.F.H., S.B.O., M.O.N., H.L., J.L., B.S.T., and D.S.; software, J.F.H.; formal analysis, J.F.H., S.B.O., M.O.N., and H.L.; investigation, J.F.H., S.B.O., M.O.N., H.L., J.L., B.S.T., and D.S.; writing, J.F.H., S.B.O., M.O.N., H.L., M.M., and C.D.; visualization, J.F.H., S.B.O., J.L., and C.D.; and supervision and funding acquisition, C.D., E.A.C., M.M., M.O.N., and S.R.

DECLARATION OF INTERESTS

In accordance with the disclosure policy, the authors (J.F.H., S.B.O., and C.D.) wish to declare that a patent application related to this work has been filed by their institution. The specific institutional reference numbers for this filing are MIT-090MUS and MIT-749AWO.

SUPPLEMENTAL INFORMATION

Supplemental information can be found online at https://doi.org/10.1016/j.device.2026.101333.

Received: May 15, 2026
Revised: September 17, 2026
Accepted: September 25, 2026

REFERENCES

1. Pardridge, W.M. (2005). The blood-brain barrier: Bottleneck in brain drug development. NeuroRx *2*, 3–14. https://doi.org/10.1602/neurorx.2.1.3.
2. Bobo, R.H., Laske, D.W., Akbasak, A., Morrison, P.F., Dedrick, R.L., and Oldfield, E.H. (1994). Convection-enhanced delivery of macromolecules in the brain. Proc. Natl. Acad. Sci. *91*, 2076–2080. https://doi.org/10.1073/pnas.91.6.2076.
3. Boyden, E.S., Zhang, F., Bamberg, E., Nagel, G., and Deisseroth, K. (2005). Millisecond-timescale, genetically targeted optical control of neural activity. Nat. Neurosci. *8*, 1263–1268. https://doi.org/10.1038/nn1525.
4. Roth, B.L. (2016). DREADDs for Neuroscientists. Neuron *89*, 683–694. https://doi.org/10.1016/j.neuron.2016.01.040.
5. Stupp, R., Mason, W.P., van den Bent, M.J., Weller, M., Fisher, B., Taphoorn, M.J.B., Belanger, K., Brandes, A.A., Marosi, C., Bogdahn, U., et al. (2005). Radiotherapy plus Concomitant and Adjuvant Temozolomide for Glioblastoma. N. Engl. J. Med. *352*, 987–996. https://doi.org/10.1056/NEJMoa043330.
6. Brem, H., Piantadosi, S., Burger, P.C., Walker, M., Selker, R., Vick, N.A., Black, K., Sisti, M., Brem, S., and Mohr, G. (1995). Placebo-controlled trial of safety and efficacy of intraoperative controlled delivery by biodegradable polymers of chemotherapy for recurrent gliomas. Lancet *345*, 1008–1012. https://doi.org/10.1016/s0140-6736(95)90755-6.
7. Valtonen, S., Timonen, U., Toivanen, P., Kalimo, H., Kivipelto, L., Heiskanen, O., Unsgaard, G., and Kuurne, T. (1997). Interstitial Chemotherapy with Carmustine-loaded Polymers for High-grade Gliomas: A Randomized Double-blind Study. Neurosurgery *41*, 44–49. https://doi.org/10.1097/00006123-199707000-00011.
8. Bastiancich, C., Malfanti, A., Préat, V., and Rahman, R. (2021). Rationally designed drug delivery systems for the local treatment of resected glioblastoma. Adv. Drug Deliv. Rev. *177*, 113951. https://doi.org/10.1016/j.addr.2021.113951.
9. Gazaille, C., Sicot, M., Saulnier, P., Eyer, J., and Bastiat, G. (2021). Local Delivery and Glioblastoma: Why Not Combining Sustained Release and Targeting? Front. Med. Technol. *3*, 791596. https://doi.org/10.3389/fmedt.2021.791596.
10. Brown, C.E., Alizadeh, D., Starr, R., Weng, L., Wagner, J.R., Naranjo, A., Ostberg, J.R., Blanchard, M.S., Kilpatrick, J., Simpson, J., et al. (2016). Regression of Glioblastoma after Chimeric Antigen Receptor T-Cell Therapy. N. Engl. J. Med. *375*, 2561–2569. https://doi.org/10.1056/nejmoa1610497.
11. Stupp, R., Taillibert, S., Kanner, A., Read, W., Steinberg, D., Lhermitte, B., Toms, S., Idbaih, A., Ahluwalia, M.S., Fink, K., et al. (2017). Effect of Tumor-Treating Fields Plus Maintenance Temozolomide vs Maintenance Temozolomide Alone on Survival in Patients With Glioblastoma: A

Randomized Clinical Trial. JAMA *318*, 2306–2316. https://doi.org/10.1001/jama.2017.18718.

12. Lonser, R.R., Sarntinoranont, M., Morrison, P.F., and Oldfield, E.H. (2015). Convection-enhanced delivery to the central nervous system. J. Neurosurg. *122*, 697–706. https://doi.org/10.3171/2014.10.jns14229.
13. Mehta, A.M., Sonabend, A.M., and Bruce, J.N. (2017). Convection-Enhanced Delivery. Neurotherapeutics *14*, 358–371. https://doi.org/10.1007/s13311-017-0520-4.
14. Lewis, O., Woolley, M., Johnson, D., Rosser, A., Barua, N.U., Bienemann, A.S., Gill, S.S., and Evans, S. (2016). Chronic, intermittent convection-enhanced delivery devices. J. Neurosci. Methods *259*, 47–56. https://doi.org/10.1016/j.jneumeth.2015.11.008.
15. White, E., Bienemann, A., Malone, J., Megraw, L., Bunnun, C., Wyatt, M., and Gill, S. (2011). An evaluation of the relationships between catheter design and tissue mechanics in achieving high-flow convection-enhanced delivery. J. Neurosci. Methods *199*, 87–97. https://doi.org/10.1016/j.jneumeth.2011.04.027.
16. Hynynen, K., McDannold, N., Vykhodtseva, N., and Jolesz, F.A. (2001). Noninvasive MR Imaging–guided Focal Opening of the Blood-Brain Barrier in Rabbits. Radiology *220*, 640–646. https://doi.org/10.1148/radiol.2202001804.
17. Lipsman, N., Meng, Y., Bethune, A.J., Huang, Y., Lam, B., Masellis, M., Herrmann, N., Heyn, C., Aubert, I., Boutet, A., et al. (2018). Blood–brain barrier opening in Alzheimer's disease using MR-guided focused ultrasound. Nat. Commun. *9*, 2336. https://doi.org/10.1038/s41467-018-04529-6.
18. Karakatsani, M.E., Blesa, J., and Konofagou, E.E. (2019). Blood–brain barrier opening with focused ultrasound in experimental models of Parkinson's disease. Mov. Disord. *34*, 1252–1261. https://doi.org/10.1002/mds.27804.
19. Zhao, P., Wu, T., Tian, Y., You, J., and Cui, X. (2024). Recent advances of focused ultrasound induced blood-brain barrier opening for clinical applications of neurodegenerative diseases. Adv. Drug Deliv. Rev. *209*, 115323. https://doi.org/10.1016/j.addr.2024.115323.
20. Wu, C.-C., Szalontay, L., Pouliopoulos, A.N., Bae, S., Berg, X., Wei, H.J., Webster Carrion, A., Kokossis, D., Sethi, C., Fino, J., et al. (2025). Blood-brain barrier opening with neuronavigation-guided focused ultrasound in pediatric patients with diffuse midline glioma. Sci. Transl. Med. *17*, eadq6645. https://doi.org/10.1126/scitranslmed.adq6645.
21. Mo, S., Coussios, C.-C., Seymour, L., and Carlisle, R. (2012). Ultrasound-enhanced drug delivery for cancer. Expert Opin. Drug Deliv. *9*, 1525–1538. https://doi.org/10.1517/17425247.2012.739603.
22. Labib, S., Bright, R.K., and Liu, J. (2025). Focused Ultrasound in Cancer Immunotherapy: A Review of Mechanisms and Applications. Ultrasound Med. Biol. *51*, 1–14. https://doi.org/10.1016/j.ultrasmedbio.2024.09.008.
23. Wang, J., Li, Z., Pan, M., Fiaz, M., Hao, Y., Yan, Y., Sun, L., and Yan, F. (2022). Ultrasound-mediated blood–brain barrier opening: An effective drug delivery system for theranostics of brain diseases. Adv. Drug Deliv. Rev. *190*, 114539. https://doi.org/10.1016/j.addr.2022.114539.
24. Bae, S., Liu, K., Pouliopoulos, A.N., Ji, R., Jiménez-Gambín, S., Yousefian, O., Kline-Schoder, A.R., Batts, A.J., Tsitsos, F.N., Kokossis, D., et al. (2024). Transcranial blood-brain barrier opening in Alzheimer's disease patients using a portable focused ultrasound system with real-time 2-D cavitation mapping. Theranostics *14*, 4519–4535. https://doi.org/10.7150/thno.94206.
25. Hu, Z., Chen, S., Yang, Y., Gong, Y., and Chen, H. (2022). An Affordable and Easy-to-Use Focused Ultrasound Device for Noninvasive and High Precision Drug Delivery to the Mouse Brain. IEEE Trans. Biomed. Eng. *69*, 2723–2732. https://doi.org/10.1109/tbme.2022.3150781.
26. Pons-Faudoa, F.P., Ballerini, A., Sakamoto, J., and Grattoni, A. (2019). Advanced implantable drug delivery technologies: transforming the clinical landscape of therapeutics for chronic diseases. Biomed. Microdevices *21*, 47. https://doi.org/10.1007/s10544-019-0389-6.
27. Nayeem, M.O.G., Viswanath, S., Yoon, H., Shah, A., Sadat, D., Marcus, C., Chandrakasan, A.P., Ozmen, T., and Dagdeviren, C. (2026). Portable, real-time 3D ultrasound for operator-independent breast imaging. Nat. Commun. *17*, 5679. https://doi.org/10.1038/s41467-026-74708-3.
28. Hou, J.F., Viswanath, S., Dilibal, C., Wu, B., Shende, T., and Dagdeviren, C. (2026). Real-time 3D ultrasound in augmented reality accelerates training and narrows novice–expert performance gaps. Commun. Eng. *5*, 107. https://doi.org/10.1038/s44172-026-00692-7.
29. Marcus, C., Nayeem, M.O.G., Shah, A., Hou, J., Viswanath, S., Eusebio, M., Sadat, D., Chandrakasan, A.P., Ozmen, T., and Dagdeviren, C. (2026). Real-Time 3D Ultrasound Imaging with an Ultra-Sparse, Low Power Architecture. Adv. Healthcare Mater. *15*, e05310. https://doi.org/10.1002/adhm.202505310.
30. Hou, J.F., Nayeem, M.O.G., Caplan, K.A., Ruesch, E.A., Caban-Murillo, A., Criado-Hidalgo, E., Ornellas, S.B., Williams, B., Pearce, A.A., Dagdeviren, H.E., et al. (2024). An implantable piezoelectric ultrasound stimulator (ImPULS) for deep brain activation. Nat. Commun. *15*, 4601. https://doi.org/10.1038/s41467-024-48748-6.
31. Du, W., Zhang, L., Suh, E., Lin, D., Marcus, C., Ozkan, L., Ahuja, A., Fernandez, S., Shuvo, I.I., Sadat, D., et al. (2023). Conformable ultrasound breast patch for deep tissue scanning and imaging. Sci. Adv. *9*, eadh5325. https://doi.org/10.1126/sciadv.adh5325.
32. Boroumand, A., Mehrarya, M., Ghanbarzadeh-Dagheyan, A., and Ahmadian, M.T. (2022). Numerical and experimental evaluation of ultrasound-assisted convection enhanced delivery to transfer drugs into brain tumors. Sci. Rep. *12*, 19299. https://doi.org/10.1038/s41598-022-23429-w.
33. Wiklund, M., Green, R., and Ohlin, M. (2012). Acoustofluidics 14: Applications of acoustic streaming in microfluidic devices. Lab Chip *12*, 2438–2451. https://doi.org/10.1039/c2lc40203c.
34. Raghavan, R. (2018). Theory for acoustic streaming in soft porous matter and its applications to ultrasound-enhanced convective delivery. J. Ther. Ultrasound *6*, 6. https://doi.org/10.1186/s40349-018-0114-6.
35. Chen, M., Zhang, B., Kim, H., Kreager, B.C., Yang, W., Zhao, K., Moon, S., Wu, H., Crosby, E.J., Osada, T., et al. (2026). Precision ultrasound-localized sonoporation equipment enabling intratumoral delivery for cancer immunotherapy. Cell Rep. Phys. Sci. *7*, 103554. https://doi.org/10.1016/j.xcrp.2026.103554.
36. Riley, N. (1965). Oscillating viscous flows. Mathematika *12*, 161–175. https://doi.org/10.1112/s0025579300005283.
37. Ergun, A.S., Yaralioglu, G.G., and Khuri-Yakub, B.T. (2003). Capacitive Micromachined Ultrasonic Transducers: Theory and Technology. J. Aero. Eng. *16*, 76–84.
38. Qiu, Y., Gigliotti, J.V., Wallace, M., Griggio, F., Demore, C.E.M., Cochran, S., and Trolier-McKinstry, S. (2015). Piezoelectric Micromachined Ultrasound Transducer (PMUT) Arrays for Integrated Sensing, Actuation and Imaging. Sensors (Basel) *15*, 8020–8041. https://doi.org/10.3390/s150408020.
39. Roy, K., Lee, J.E.-Y., and Lee, C. (2023). Thin-film PMUTs: a review of over 40 years of research. Microsyst. Nanoeng. *9*, 95. https://doi.org/10.1038/s41378-023-00555-7.
40. Dagdeviren, C., Ramadi, K.B., Joe, P., Spencer, K., Schwerdt, H.N., Shimazu, H., Delcasso, S., Amemori, K.I., Nunez-Lopez, C., Graybiel, A.M., et al. (2018). Miniaturized neural system for chronic, local intracerebral drug delivery. Sci. Transl. Med. *10*, eaan2742. https://doi.org/10.1126/scitranslmed.aan2742.
41. Pardridge, W.M. (2011). Drug transport in brain via the cerebrospinal fluid. Fluids Barriers CNS *8*, 7. https://doi.org/10.1186/2045-8118-8-7.
42. Carpentier, A., Stupp, R., Sonabend, A.M., Dufour, H., Chinot, O., Mathon, B., Ducray, F., Guyotat, J., Baize, N., Menei, P., et al. (2024). Repeated blood–brain barrier opening with a nine-emitter implantable ultrasound device in combination with carboplatin in recurrent glioblastoma: a phase I/II clinical trial. Nat. Commun. *15*, 1650. https://doi.org/10.1038/s41467-024-45818-7.

Please cite this article in press as: Hou et al., Long-term ultrasound-enhanced convective injection device for neural drug delivery, Device (2026), https://doi.org/10.1016/j.device.2026.101333

43. Mast, T.D. (2000). Empirical relationships between acoustic parameters in human soft tissues. Acoust Res. Lett. Online *1*, 37–42. https://doi.org/10.1121/1.1336896.

44. Lighthill, S.J. (1978). Acoustic streaming. J. Sound Vib. *61*, 391–418. https://doi.org/10.1016/0022-460x(78)90388-7.

45. Wellman, S.M., and Kozai, T.D.Y. (2017). Understanding the Inflammatory Tissue Reaction to Brain Implants To Improve Neurochemical Sensing Performance. ACS Chem. Neurosci. *8*, 2578–2582. https://doi.org/10.1021/acschemneuro.7b00403.

46. Sohal, H.S., Clowry, G.J., Jackson, A., O'Neill, A., and Baker, S.N. (2016). Mechanical Flexibility Reduces the Foreign Body Response to Long-Term Implanted Microelectrodes in Rabbit Cortex. PLoS One *11*, e0165606. https://doi.org/10.1371/journal.pone.0165606.

47. Apollo, N.V., Murphy, B., Prezelski, K., Driscoll, N., Richardson, A.G., Lucas, T.H., and Vitale, F. (2020). Gels, jets, mosquitoes, and magnets: a review of implantation strategies for soft neural probes. J. Neural. Eng. *17*, 041002. https://doi.org/10.1088/1741-2552/abacd7.

48. Zhao, H., Liu, R., Zhang, H., Cao, P., Liu, Z., and Li, Y. (2022). Research Progress on the Flexibility of an Implantable Neural Microelectrode. Micromachines *13*, 386. https://doi.org/10.3390/mi13030386.

49. Chen, P.-C., Young, C.G., Schaffer, C.B., and Lal, A. (2022). Ultrasonically actuated neural probes for reduced trauma and inflammation in mouse brain. Microsyst. Nanoeng. *8*, 117. https://doi.org/10.1038/s41378-022-00438-3.

50. Chen, Z.-J., Gillies, G.T., Broaddus, W.C., Prabhu, S.S., Fillmore, H., Mitchell, R.M., Corwin, F.D., and Fatouros, P.P. (2004). A realistic brain tissue phantom for intraparenchymal infusion studies. J. Neurosurg. *101*, 314–322. https://doi.org/10.3171/jns.2004.101.2.0314.

51. Márton, G., Tóth, E.Z., Wittner, L., Fiáth, R., Pinke, D., Orbán, G., Meszéna, D., Pál, I., Győri, E.L., Bereczki, Z., et al. (2020). The neural tissue around SU-8 implants: A quantitative in vivo biocompatibility study. Mater. Sci. Eng. C *112*, 110870. https://doi.org/10.1016/j.msec.2020.110870.

52. Liu, F., and Fu, T.-M. (2025). Material and design strategies for chronically-implantable neural probes. NPG Asia Mater. *17*, 32. https://doi.org/10.1038/s41427-025-00613-8.

53. Aubry, J.-F., Attali, D., Schafer, M.E., Fouragnan, E., Caskey, C.F., Chen, R., Darmani, G., Bubrick, E.J., Sallet, J., Butler, C.R., et al. (2025). ITRUSST consensus on biophysical safety for transcranial ultrasound stimulation. Brain Stimul. *18*, 1896–1905. https://doi.org/10.1016/j.brs.2025.10.007.

54. Shaw, A., Ter Haar, G., Haller, J., and Wilkens, V. (2015). Towards a dosimetric framework for therapeutic ultrasound. Int. J. Hyperther. *31*, 182–192. https://doi.org/10.3109/02656736.2014.997311.

55. U.S. Food and Drug Administration (2023). Center for Devices and Radiological Health. Marketing Clearance of Diagnostic Ultrasound Systems and Transducers: Guidance for. Industry and Food and Drug Administration Staff, 14–17.. http://www.fda.gov/media/71100/download.

56. Huang, S.-H., Lin, S.-P., and Chen, J.-J.J. (2014). In vitro and in vivo characterization of SU-8 flexible neuroprobe: From mechanical properties to electrophysiological recording. Sensor Actuator Phys. *216*, 257–265. https://doi.org/10.1016/j.sna.2014.06.005.

57. UpNano GmbH. UpNano Material Brochure: Resin Portfolio for Demanding Applications. https://www.upnano.com/wp-content/uploads/2024/01/UpNano_Material_Brochure.pdf (2026).

58. Arrieta, V.A., Gould, A., Kim, K.S., Habashy, K.J., Dmello, C., Vázquez-Cervantes, G.I., Palacín-Aliana, I., McManus, G., Amidei, C., Gomez, C., et al. (2024). Ultrasound-mediated delivery of doxorubicin to the brain results in immune modulation and improved responses to PD-1 blockade in gliomas. Nat. Commun. *15*, 4698. https://doi.org/10.1038/s41467-024-48326-w.

59. Maruo, S., Nakamura, O., and Kawata, S. (1997). Three-dimensional microfabrication with two-photon-absorbed photopolymerization. Opt. Lett. *22*, 132–134. https://doi.org/10.1364/ol.22.000132.

60. Theeuwes, F. (1975). Elementary Osmotic Pump. J. Pharm. Sci. *64*, 1987–1991. https://doi.org/10.1002/jps.2600641218.

61. Mickle, A.D., Won, S.M., Noh, K.N., Yoon, J., Meacham, K.W., Xue, Y., McIlvried, L.A., Copits, B.A., Samineni, V.K., Crawford, K.E., et al. (2019). A wireless closed-loop system for optogenetic peripheral neuromodulation. Nature *565*, 361–365. https://doi.org/10.1038/s41586-018-0823-6.

62. Hoang, M.D., Kang, W., Koh, M., and Park, S.-M. (2025). Fully Wireless Implantable Device Capable of Multichannel Neural Spike Recording and Stimulation for Long-Term Freely Moving Rodent Study. IEEE Trans. Neural Syst. Rehabil. Eng. *33*, 1621–1632. https://doi.org/10.1109/tnsre.2025.3564625.

63. Piangerelli, M., Ciavarro, M., Paris, A., Marchetti, S., Cristiani, P., Puttilli, C., Torres, N., Benabid, A.L., and Romanelli, P. (2014). A Fully Integrated Wireless System for Intracranial Direct Cortical Stimulation, Real-Time Electrocorticography Data Transmission, and Smart Cage for Wireless Battery Recharge. Front. Neurol. *5*, 156. https://doi.org/10.3389/fneur.2014.00156.

64. Del Bono, F., Bontempi, A., Dentis, A., Trani, N.D., Demarchi, D., Grattoni, A., and Ros, P.M. (2024). Design of a Closed-Loop Wireless Power Transfer System for an Implantable Drug Delivery Device. IEEE Sens. J. *24*, 7345–7354. https://doi.org/10.1109/jsen.2023.3270521.

65. Gendron, P.-O., Avaltroni, F., and Wilkinson, K.J. (2008). Diffusion Coefficients of Several Rhodamine Derivatives as Determined by Pulsed Field Gradient–Nuclear Magnetic Resonance and Fluorescence Correlation Spectroscopy. J. Fluoresc. *18*, 1093–1101. https://doi.org/10.1007/s10895-008-0357-7.

66. Nicholson, C., and Tao, L. (1993). Hindered diffusion of high molecular weight compounds in brain extracellular microenvironment measured with integrative optical imaging. Biophys. J. *65*, 2277–2290. https://doi.org/10.1016/s0006-3495(93)81324-9.

67. Toscano, J.D., Guo, Y., Wang, Z., Vaezi, M., Mori, Y., Karniadakis, G.E., Boster, K.A.S., and Kelley, D.H. (2026). MR-AIV reveals in vivo brain-wide fluid flow with physics-informed AI. Sci. Adv. *12*, eaeb0404. https://doi.org/10.1126/sciadv.aeb0404.